29th AIAA Applied Aerodynamics Conference
27 - 30 June 2011, Honolulu, Hawaii

AIAA 2011-3339

Computational Challenges in Simulating Powered Flight of the Orion Launch Abort Vehicle

Stuart E. Rogers* and Thomas H. Pulliam*
NASA Ames Research Center, Moffett Field, CA, 94035, U.S.A.

Some of the simulation work performed by the computational aerosciences project under the NASA Constellation program is presented. The challenges of simulating the powered flight of the Orion launch abort vehicle for the purposes of building an aerodynamics database are discussed. During an abort this vehicle fires both a four-nozzle abort motor together with an eight-nozzle attitude control motor. The interactions of the jet plumes provide a significant challenge to the computational tools. A few of the computed results using overset grids and the Overflow solver are presented. Some very complex behavior in the jet plumes was observed, including asymmetric yaw-inducing plume interactions. The problem of jet-plume simulation was studied using a simpler jet-in-crossflow problem. A number of these simulations also produce asymmetric results for a completely symmetric problem. The results from the use of different turbulence models, different grid resolution, and various differencing schemes are presented for the jet-in-crossflow problem. All steady-state cases are shown to be asymmetric, while time-averaged solutions from time-accurate simulations are symmetric.

Nomenclature

α	angle of attack
γ	ratio of specific heats
ω	specific turbulence dissipation variable
C_A	axial force coefficient
C_N	normal force coefficient
C_P	specific heat at constant pressure
C_p	pressure coefficient
C_Y	side force coefficient
C_{p0}	total pressure coefficient
k	turbulence kinetic energy
R	gas constant
ACM	Attitude Control Motor
AM	Abort Motor
BB	Baldwin-Barth turbulence model
CFD	computational fluid dynamics
FMG	full multi-grid
HLLC	Harten Lax van Leer Contact reimann solver
HLLE++	Harten Lax van Leer Einfeldt reimann solver
J	jet-to-freestream dynamic pressure ratio
LAV	Launch Abort Vehicle
RANS	Reynolds-averaged Navier-Stokes
SA	Spalart-Allmaras turbulence model
SST	Shear-stress transport turbulence model

*Aerospace Engineer, NASA Supercomputing Division, Mail Stop 258-2, Associate Fellow AIAA

I. Introduction

The launch abort system being designed for the ascent of the Orion space vehicle provides a significant challenge to aerodynamicists and design engineers. The launch abort vehicle (LAV) is equipped with an abort motor (AM) with four down-firing nozzles, an attitude-control motor (ACM) with eight circumferentially arranged side-firing jets each controlled through a pintle nozzle, and a jettison motor. During an abort, the AM and ACM are firing simultaneously and the vehicle is undergoing significant acceleration, and will experience a wide range of freestream conditions. The vehicle is designed to be capable of performing an abort at subsonic speeds, transonic speeds at maximum dynamic pressure, and at supersonic speeds.

The computational aerosciences project under the NASA Constellation program was tasked with building an aerodynmic database for the Orion LAV. The challenge was to build an aerodynamic database to model the performance of the vehicle during the firing of the abort motor. There are a large number of independent variables in such a database. In addition to the free-stream flow conditions (angle of attack, side-slip angle, Mach number, and abort altitude and trajectory), there are design variables governing the AM thrust ratio, the ACM thrust ratio, the thrust direction, and the thrust distribution amoungst the eight ACM nozzles. In addition, the aerodynamic interference due to the proximity of the LAV to the service module must be taken into account.

The aerodynamic database utilized data from both computational fluid dynamics (CFD) simulations and from and wind-tunnel tests. In both CFD and the wind tunnel, the flight during the firing of the AM was modeled with a large number of of steady-state cases to cover the flight envelope and operating range of the motors. Tens of thousands of both CFD cases and wind-tunnel cases were run in order to build this database. Several different CFD codes are being used. These include the Cart3D[1–5] flow solver, a Cartesian unstructured-grid Euler solver, the Overflow[6–9] code, which uses a structured overset-grid approach and solves the Reynolds-averaged Navier-Stokes (RANS) equations, and the USM3D[10] code, an unstructured RANS solver. The STAR computer code from the CD-adapco company was also used to predict AM and ACM internal flows and provide discharge coefficients.

The use of supersonic jets for aerodynamic control of a vehicle can lead to downstream interactions that either amplify or attenuate the forces and moments used to control the vehicle. Upon exiting the nozzle, the jet plume will turn downstream and can change the surface pressure on the aft part of the vehicle and its control surfaces. In the case of the AM plumes, they can interact with the aft portion of the vehicle. In the case of the ACM plumes, they interact not only with the vehicle, but also with the AM plumes, and can change the interaction of the AM plumes and the vehicle.

This paper will focus on the asymmetries found in the ACM plumes, and the investigations as to their cause. We present the efforts to make certain that these results were not due to an input error or a software error, and to ascertain if these results were physical or numerical in nature. In addition to investigating the LAV plume-driven flowfields, a simpler validation case was selected and studied. The case of a supersonic jet in a subsonic crossflow was studied. This work was designed to simulate the experiments of Beresh et al.[11–16] Even this relatively simple case can be a significant challenge to simulate accurately. As reported by the investigators,[15] a measureable degree of asymmetry was observed in the counter-rotating vortex pair.

Results from the jet-in-crossflow case will be presented first. The CFD results from this jet-in-crossflow case are compared with experimental results. The results of a grid-refinement study are presented, and a comparison of several differencing schemes is made, as well as a comparison of the results from different turbulence models. Computational results comparing steady-state solutions to unsteady time-accurate runs are also made. Finally, the paper will present some results from the simulations of the powered LAV, and will illustrate how complicated some of the jet interactions can be.

II. Jet in Cross-Flow Simulations

A supersonic jet in a subsonic cross-flow was simulated as a validation case for the current work. In experiments of Beresh et al,[11–14] an axisymmetric supersonic jet was exhausted transversely into a wind-tunnel with a of 12-inch square cross-section. The nozzle which forms the jet had an exit diameter of 0.375 inches and an expansion half angle of 15 degrees. The resulting experimental data includes pressure-tap data from inside the nozzle and the surrounding wind-tunnel wall and particle-image velocimetry data in the wake of the jet plume. This flow is characterized by a formation of counter-rotating vortices as the jet-plume bends downstream, together with a horseshoe vortex that forms at the base of the jet and travels

downstream next to the wall.

The experiment was run for reference Mach numbers of 0.5, 0.6, 0.7, and 0.8. The strength of the jet was measured by J, the ratio of the jet dynamic pressure to the freestream dynamic pressure. In the experiment jet ratios (J) were run with values of 2.8, 5.6, 10.2, and 16.7. The CFD simulations will focus on the baseline case of Mach=0.8 and J=10.2. In the CFD simulations, all flow quantities were specified at the nozzle inflow plane on the subsonic side, upstream of the sonic throat. The conditions where constructed to match the total pressure and temperature in the experiment for each jet strength using isentropic relations for the ratio between the throat and inflow areas.

The Overflow code was used for all computations in this work. Overflow uses a finite-difference approach and overset meshing to solve the RANS equations. The distributed memory build of this solver uses MPI message passing for communicating inter-zonal boundary data. Load balancing is obtained by splitting and distributing the zones among all CPUs allocated to a job. A number of different options are available in the Overflow solver. In the initial calibration cases and grid-resolution cases, the second-order central differencing and scalar dissipation option was used, together with the approximate factorization implicit solver. A comparison between different discretization options and different implicit solvers was made and the results are discussed in a subsequent section. The Spalart-Allmaras (SA) turbulence model[17] was used for these cases. A comparison between different turbulence models was performed and the details are presented in a subsequent section. Initially all cases were run to a steady-state solution. These cases were initialized using a full-multigrid (FMG) sequence start-up procedure using two levels of grid coarsening for 1500 time steps. The cases were then run another 5000 or more iterations were enough to obtain a steady-state solution.

An overset grid system was developed for this flow field. A pair of body-fitted zones were used to resolve the flow through the nozzle, from the upstream subsonic side of the throat and overlapping with the wind-tunnel zones. Three zones were used to model the wind-tunnel, from 60 inches upstream of the nozzle to 70 inches downstream of the nozzle. Two more Cartesian zones were added to resolve the jet plume and wake. The coordinate system in the computational domain was oriented with the X-axis aligned with the tunnel flow direction, the Z-axis aligned with the nozzle axis of symmetry, and the Y-axis transverse to the tunnel flow. The origin was placed on the axis of symmetry of the nozzle in the plane of the wind-tunnel wall containing the nozzle.

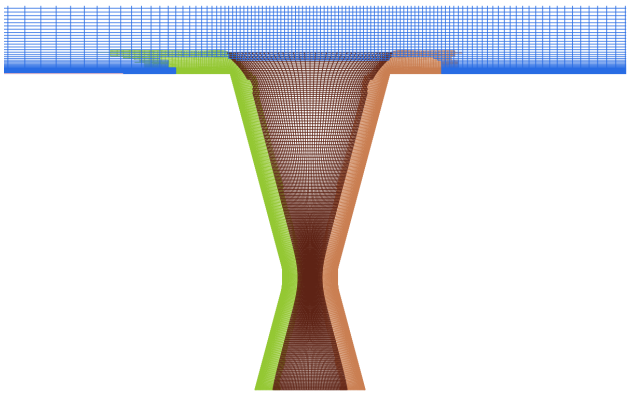

Figure 1. View of grids in the Y=0 plane of the jet nozzle.

Figure 1 shows a close view of the grids in the Y=0 plane. The wind-tunnel wall in which the nozzle was embedded was treated as a viscous surface in the test section, and was treated as an inviscid wall upstream of the nozzle. The other wind-tunnel walls were treated as slip inviscid walls, and were canted inward slightly to account for the growth of the boundary-layer displacement thickness in the tests. The boundary condition at the wind-tunnel inflow specified a constant total pressure and total temperature, and extrapolated the mass flow. The boundary condition at the wind-tunnel exit used a specified static pressure. These inflow and outflow conditions were calibrated as described below.

Both a full-body and a half-body grid system was produced. The full-body system includes the entire wind-tunnel domain, whereas the half-body grids include only one side of the symmetry plane running through the center of the jet nozzle. The half-body case uses a symmetry boundary condition on this Y=0 center plane, thus forcing the solution to be symmetric. Steps were taken to ensure that the full-body grid system was symmetric about the center plane. The grid coordinates on one side were mirrored to the opposing side of the symmetry plane. The pegasus5[18] software was modified by adding an option in which it forces the output interpolation stencils to be symmetric about the center plane.

Tunnel-empty simulations were performed to calibrate the computational model of the wind-tunnel using data published by Beresh et al.[16] The calibration runs were used to determine the appropriate static pressure at the outflow boundary for each desired Mach number in the test section. The upstream location of the

start of the inviscid-wall canting and the canting angle were varied in order to match the measured pressure distribution through the wind tunnel in the experiment. Also, the location of the start of the viscous-wall boundary condition was varied until the incoming boundary-layer displacement thickness matched that of the experiment. The calibration of each of these parameters were dependent upon the desired Mach number, and the effect of each of these parameters was not independent, and thus a significant number of parametric runs was required to complete the calibration. The post-processing and calculation of non-dimensional results used reference quantities extracted from the solution at a point 6.63 inches upstream of the jet and in the center point of the test section, which is where the experiment measured their reference quantities.

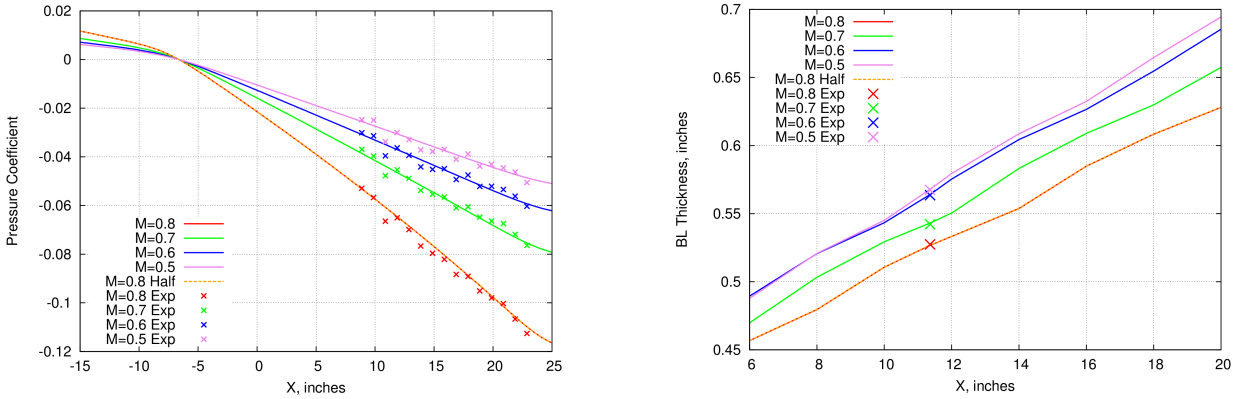

(a) C_p (b) Boundary-layer thickness

Figure 2. C_p and boundary-layer thickness versus X for tunnel-empty calibration runs.

Figure 2 show the results of the tunnel-empty calibration runs for the Mach numbers of 0.5, 0.6, 0.7, and 0.8. Also included is a half-body run for the Mach=0.8 case in which a plane of symmetry boundary condition is placed in the center of the tunnel. The first of these figures shows C_p versus the stream-wise component x, and the second plots the boundary-layer thickness versus x. These show that the calibrated CFD model compares very well with the experimental measurements, and that the half-body match the full-body results.

Cases were first run using the entire domain and no assumption of symmetry. These cases tended to produce steady-state results which were either mildly asymmetric to extremely asymmetric. The baseline case at Mach=0.8 and J=10.2 converged to a steady state as shown in figure 3. This shows plots of the three coefficients of force per square inch acting on the wind-tunnel wall versus iteration number, together with the L_2 norm of the residual in the flow solver. The three components of the force coefficients are the wind-tunnel axial force (C_A), the force in the direction normal to the floor (C_N), and the side-force (C_Y). The forces converge to a steady state, and the L_2 norm of the residual drops below 10^{-9}. The asymmetry in this solution is illustrated in figure 4(a). This figure shows Mach contours in the X=5.0 inch plane together with a semi-transparent iso-surface of Mach=0.7. This shows an asymmetry in the orientation of the higher-speed jet flow, and an even bigger asymmetry in the formation of the horseshoe vortex near the wall.

Efforts were made to determine if the asymmetry was numerical or physical in nature: were these solutions valid solutions to the Navier-Stokes equations, or were they due to an error in the software, the inputs, or some unknown influence? A number of flow-solver inputs were varied to explore the possible solutions. In one such run the full-multi-grid startup sequencing was turned off. Interestingly, this resulted in a solution which appeared to be the mirror image of the first solution shown in figure 4(a). This new solution without FMG is shown in figure 4(b). The two images in figure 5 are contours of the v-component of velocity in the center plane for the results with and without FMG. These two images clearly illustrate that the two solutions are reflections of each other about the center plane. The fact that there are two stable, steady-state solutions that are mirror images of each other provides evidence that the asymmetry is not caused by a numerical or input error which biases or pushes the solution to only one side.

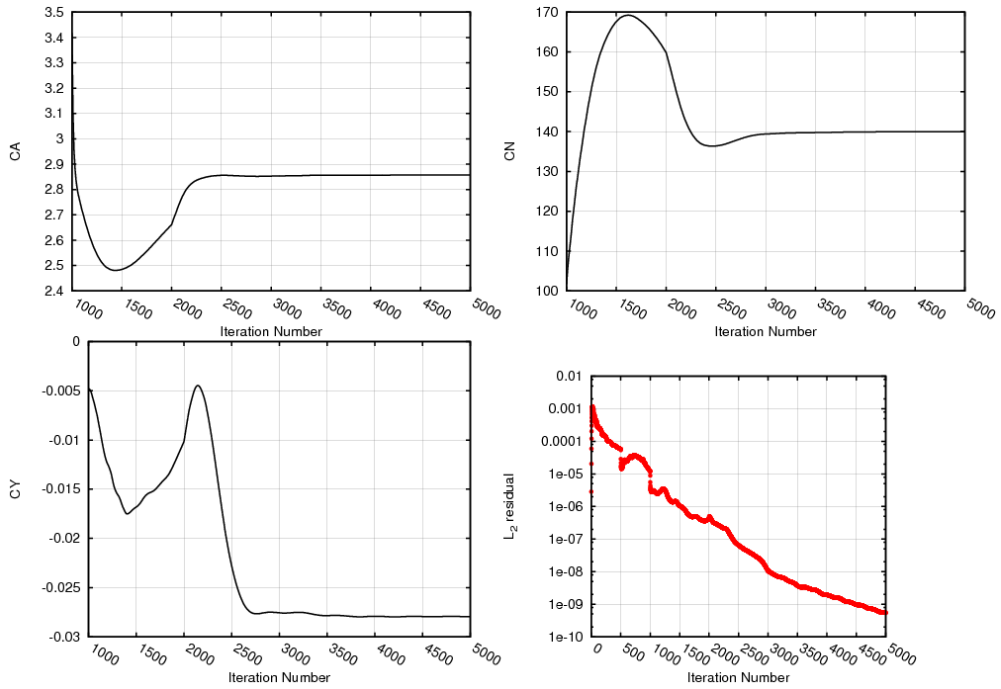

Figure 3. Convergence of the wind-tunnel floor force coefficients and the L_2 norm of the residual for Mach=0.8 and J=10.2.

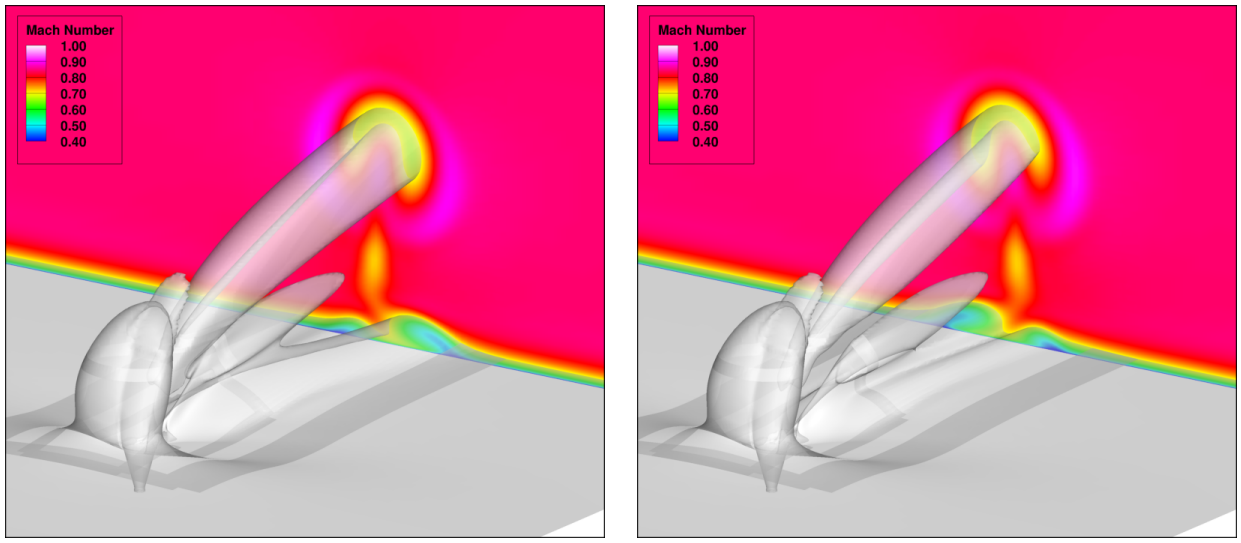

(a) FMG on (b) FMG off

Figure 4. Mach number contours at X=5.0 inches together with Mach=0.7 iso-surfaces for Mach=0.8 and J=10.2.

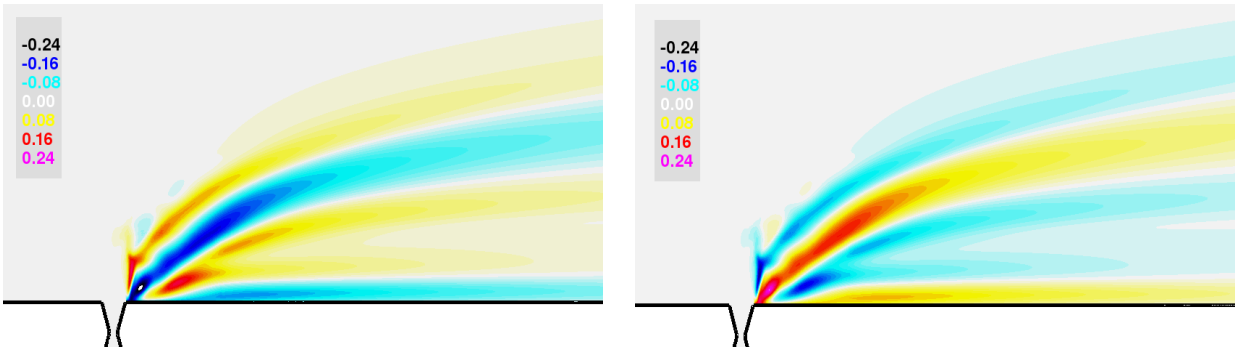

(a) FMG on

(b) FMG off

Figure 5. Contours of v-velocity component in the center plane for cases run with and without FMG sequencing at Mach=0.8 and J=10.2.

The half-body geometry was also run for the Mach=0.8 and J=10.2 case. Figure 6 illustrates the Mach contours and iso-surfaces for this case. The flow structure appears similar to the left-half of the full-body case, but with small differences due to the asymmetry in the full-body solution. Plots of velocity deficit in the center plane at streamwise stations 7.88, 9.83, 11.81, 13.75, and 15.75 inches downstream of the jet nozzle are shown in figure 7, comparing the half-body, full-body, and experimental measurements. The streamwise velocity deficit is defined to be $(U_{edge} - u)/U_{ref}$, where U_{edge} is the u-component of velocity six inches from the nozzle wall at the profile location; u is the local u-component of velocity, and U_{ref} is the u-component of the reference velocity. These profiles show that there are minor differences between the full- and half-body results, and between the computational and experimental data. There is good agreement in the data as to the location and strength of the velocity deficit in the wake of the plume that is about three inches above the nozzle wall in the first profile. The full-body results tend to predict a higher location than the half-body results, which matches the experiment. The additional deficit in velocity seen about one inch above the nozzle wall in the computational results is not seen in the experimental data.

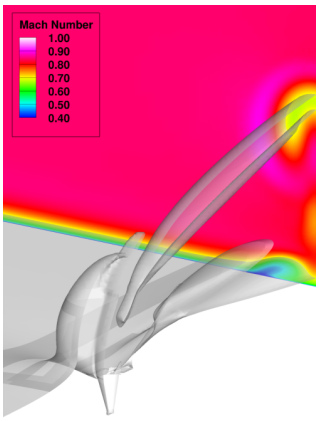

Figure 6. Mach number contours at X=5.0 inches together with Mach=0.7 iso-surfaces for the half-body geometry at Mach=0.8 and J=10.2.

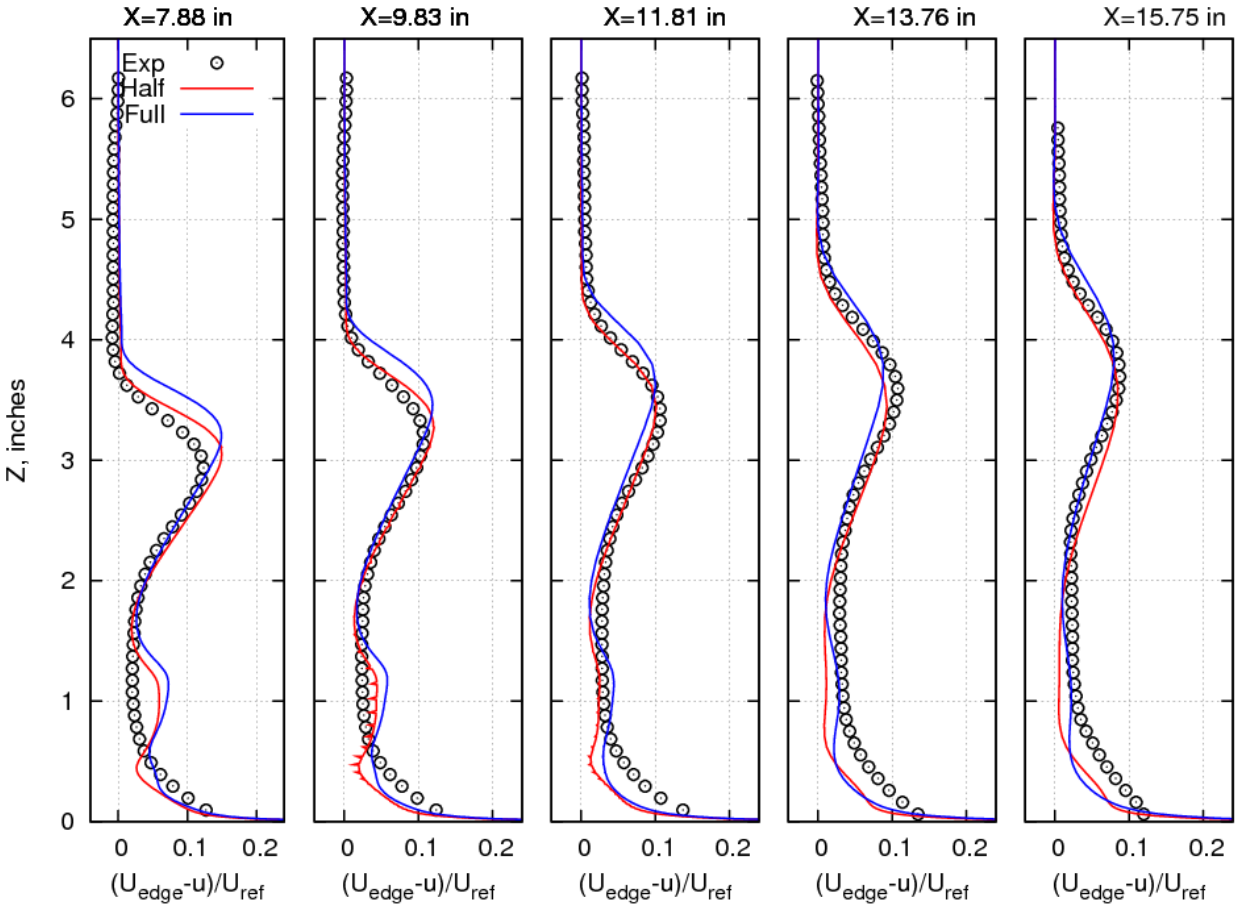

Figure 7. Velocity-deficit profiles for the half- and full-body geometry at Mach=0.8 and J=10.2.

A. Grid-Resolution Study

A grid resolution study was undertaken using four different grid systems of varying grid density. The baseline grid system that was used in all of the preceding results consisted of 7.1 million grid points. Three successively finer grids were generated using 12.2, 24.9, and 40.7 million grid points, referred to as the F2, F4, and F8 grid systems, respectively. The grid-resolution cases were run using Mach=0.8, J=10.2, and the SA turbulence model.

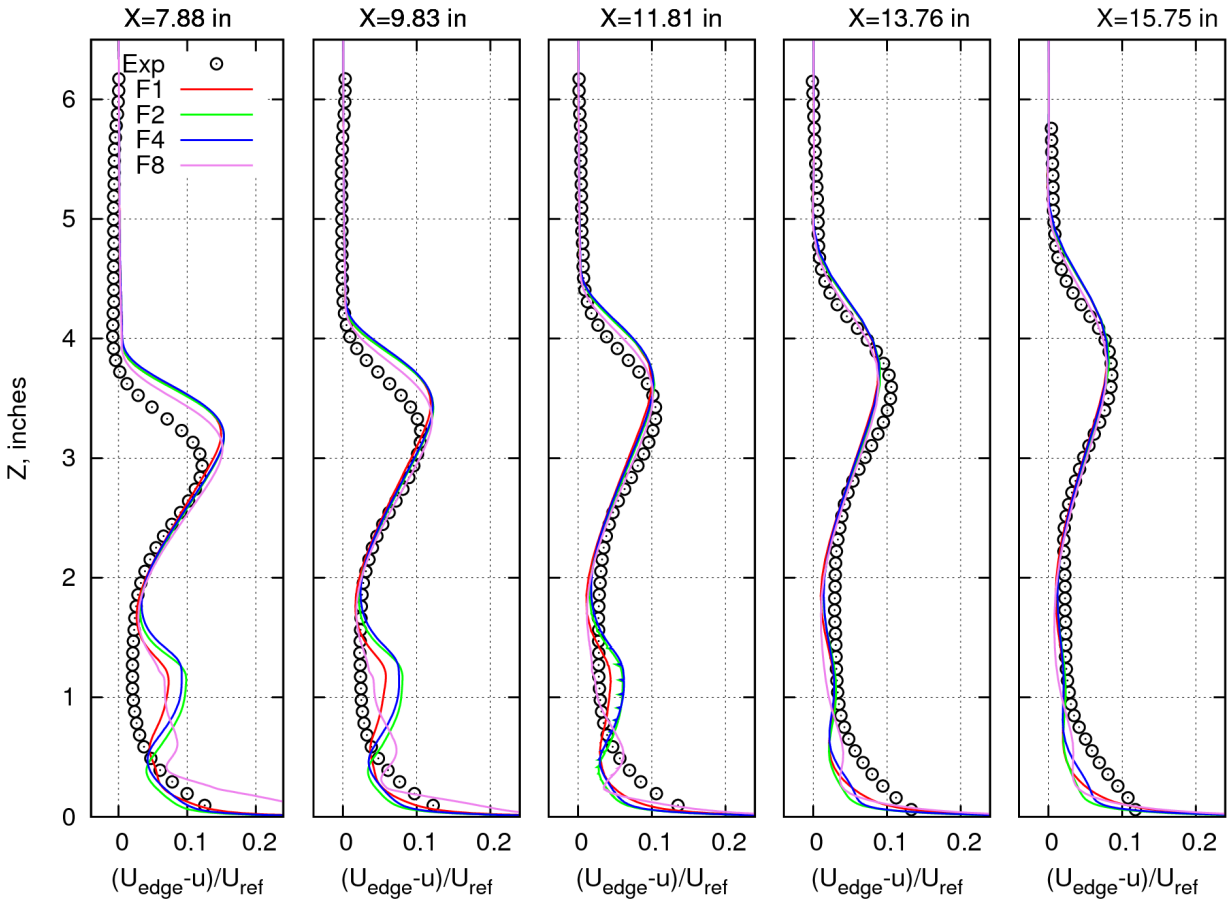

Figure 8. Velocity-deficit profiles for the grid-resolution calculations.

The results of these cases are shown in figure 8 which plots the velocity deficit versus the distance from the wall. Figure 9 plots the w-component of velocity versus the distance from the wall. The plots indicate that these calculations do not converge to a grid-independant solution. Further viewing of these flow fields in figure 10 shows that the differences in the velocity profiles are due to a differences in the asymmetries in the solutions. In particular, the F8 grid solution shows the greatest asymmetry, with more rolling of the plume wake compared to the other solutions. Thus the difference in the F8 velocity profiles is not due to a difference in the shear layer of the plume, but rather due to the difference in roll angle. This illustrates how difficult it is to validate this flowfield with just data extracted from the Y=0 plane when each of the simulations predict a slightly different asymmetry and a different amount of roll to the jet plume.

B. Differencing Scheme Study

Cases were run using three additional differencing schemes in the Overflow code. These include a third-order Roe upwind scheme, the Harten, Lax, van Leer, contact reimann solver (HLLC) upwind scheme, and the Harten, Lax, van Leer, Einfeldt reimann solver (HLLE++) upwind scheme. These schemes and their implementation into Overflow are discussed in the work by Tramel et al.[19] These cases do not converge as rapidly to a steady-state. The HLLE++ case in particular does not converge even after it was run for

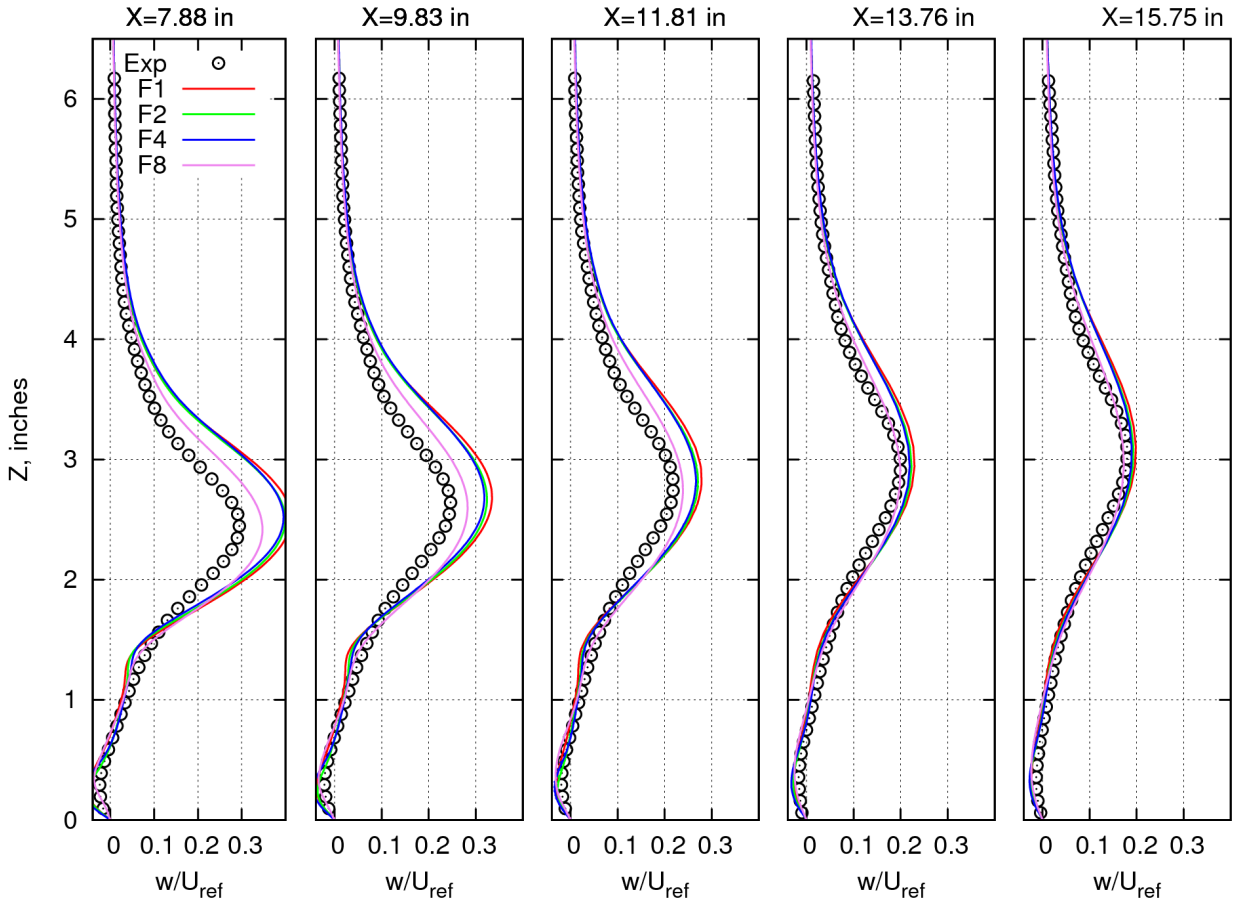

Figure 9. Z-component of velocity profiles for the grid-resolution calculations.

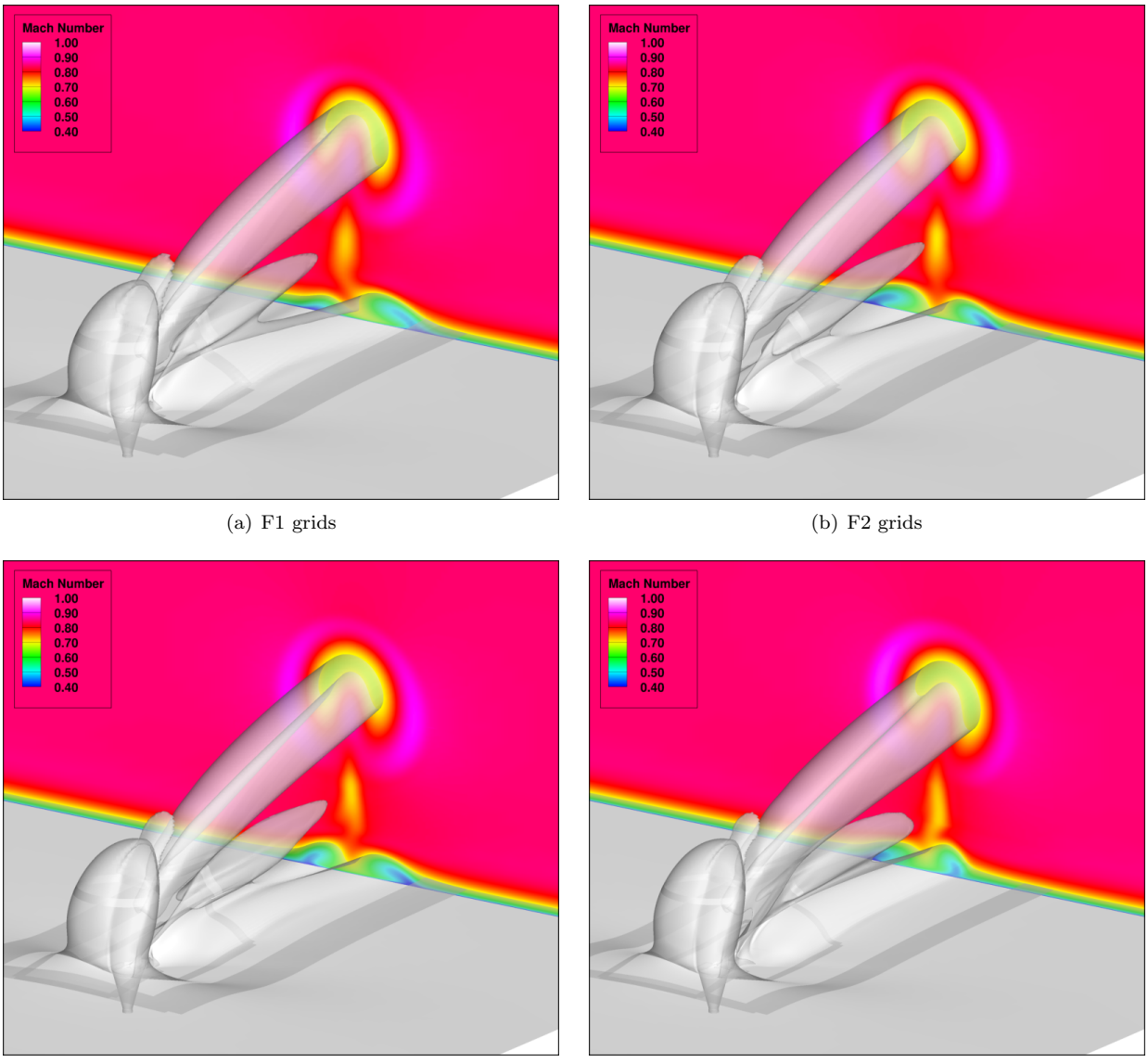

(a) F1 grids

(b) F2 grids

(c) F4 grids

(d) F8 grids

Figure 10. Flowfield images for the grid-resolution cases using the F1, F2, F4, and F8 grids at Mach=0.8 and J=10.2.

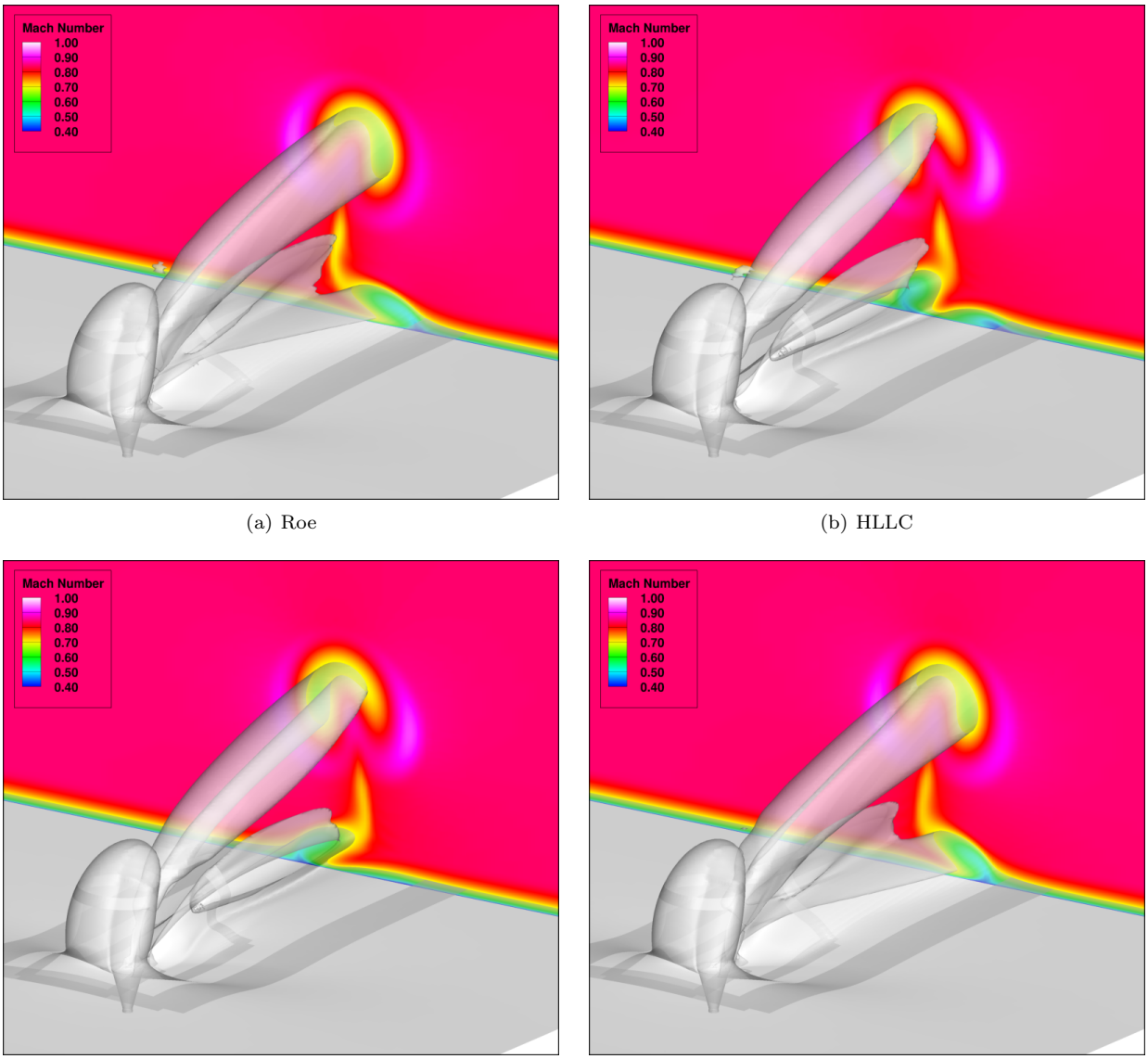

(a) Roe

(b) HLLC

(c) HLLE++ at 24,000 iterations

(d) HLLE++ at 36,000 iterations

Figure 11. Flow solutions for the Roe upwind scheme, the HLLC upwind scheme, and the HLLE++ scheme at 24,000 and 36,000 iterations.

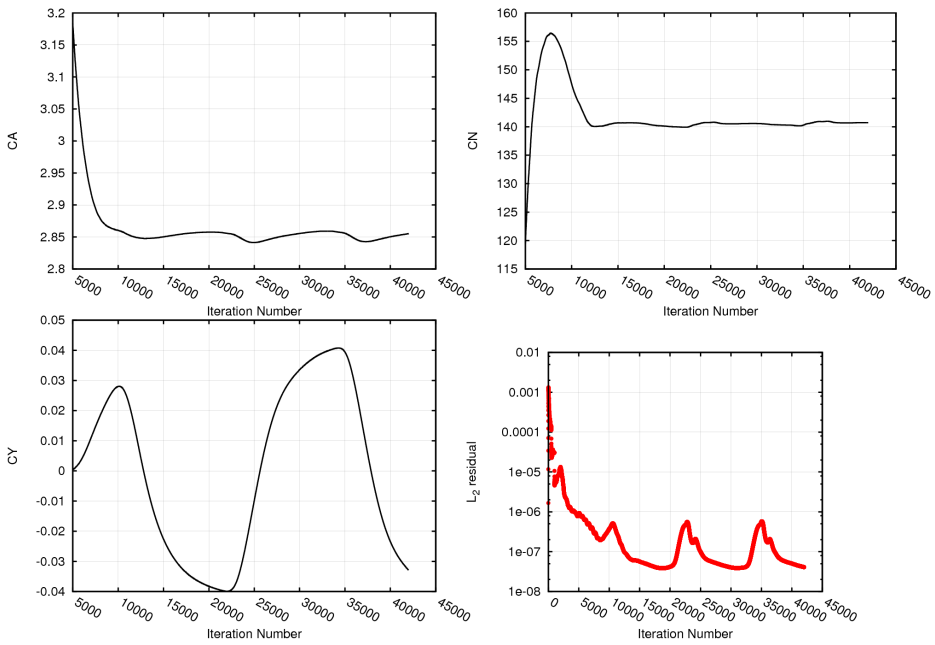

Figure 12. Convergence of the wind-tunnel Z=0 wall force coefficients and the L_2 norm of the residual for the HLLE++ upwind differencing scheme at Mach=0.8 and J=10.2.

42,000 iterations. The flow-field plots for these cases are shown in figure 11. The HLLE++ solution is plotted at two different iterations to show that it appears to be oscillating between two mirror asymmetric conditions. Figure 12 plots the force coefficients acting on the Z=0 wind-tunnel wall together with the L_2 norm of the residual for the HLLE++ case. This figure shows the C_Y data oscillating between postive and negative values, showing that the solution oscillates back and forth between two asymmetric states, one where the plume rolls to the left, one where the plume rolls to the right. Since this case was simulated in a steady-state mode, there are time-integration inaccuracies in this solution, but this does serve to illustrate a strong tendancy to remain unsteady.

C. Turbulence Model Study

Cases were run with three additional turbulence models: the Baldwin-Barth (BB) one-equation model,[20] the $k-\omega$ two-equation model,[21] and the Mentor shear-stress transport (SST) two-equation model.[22] These were all run with central differncing and scalar dissipation. The plots comparing the flow field of all four turbulence models are shown in figure 13. It can be seen that each of these solutions look considerably different. In particular, the $k-\omega$ plume has rolled over enough to interact with and lift one leg of the horseshoe vortex up and off the wall. The Baldwin-Barth computation never converged to a steady-state and behaved in a similar fashion to the HLLE++ computation in that the side-force coefficient data oscillated between positive and negative values, and the plume oscillated back and forth. The other turbulence model computations all converged to a steady state. Figure 14 contains the velocity-deficit profiles for the four turbulence model cases. As expected from the flow-field plots, there is a big discrepancy in the velocity data between the different models, and none of them agree very well with the experimental data, except for the SA model. Figure 15 contains the profiles of the w-component of velocity for the four models. In this case they all predict too much upward velocity in the core of the plume, with the execption of the $k-\omega$ results.

D. Time-Accurate Computations

The HLLE++ and Baldwin-Barth solutions suggest that this flow has a tendancy to become unsteady and periodic in time. The differences seen in the turbulence model and differencing schemes solutions suggest that this flow field and the asymmetric behavior of jet plume is dependant on the dissipation provided by the eddy viscosity and the differencing scheme. In addition, running the cases with the steady-state solver

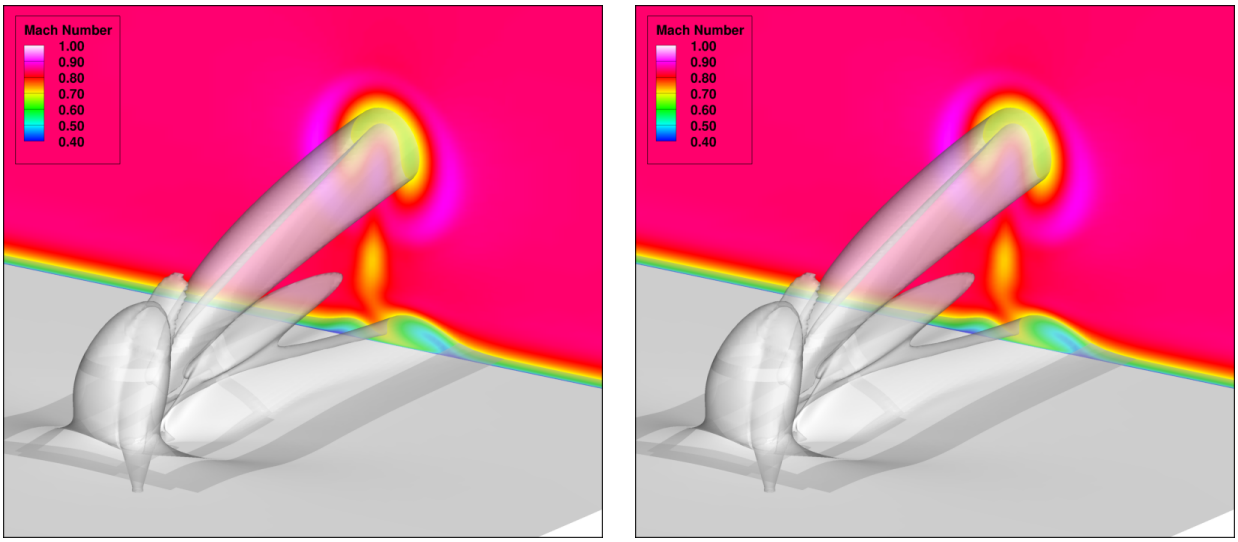

(a) SA Model

(b) BB Model

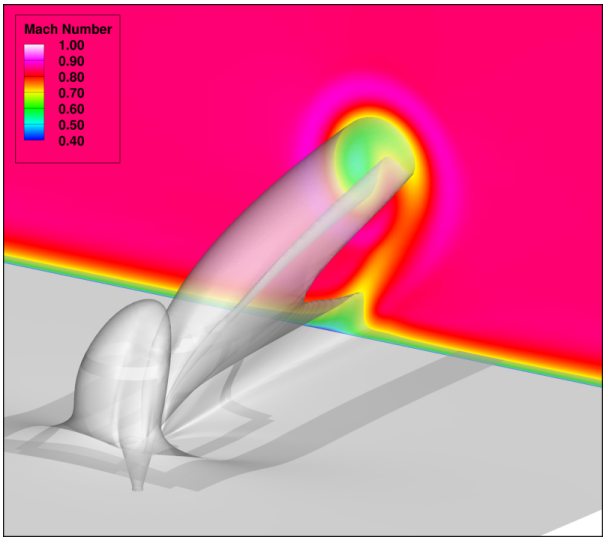

(c) $k-\omega$ Model

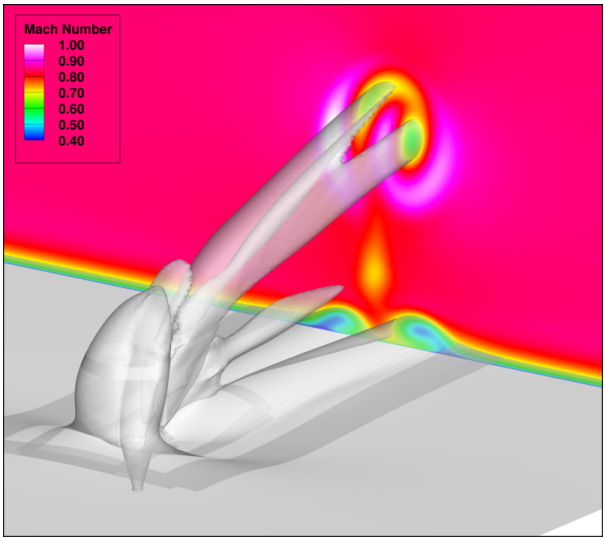

(d) SST Model

Figure 13. Flow solutions for the SA, BB, $k-\omega$, and SST turbulence models.

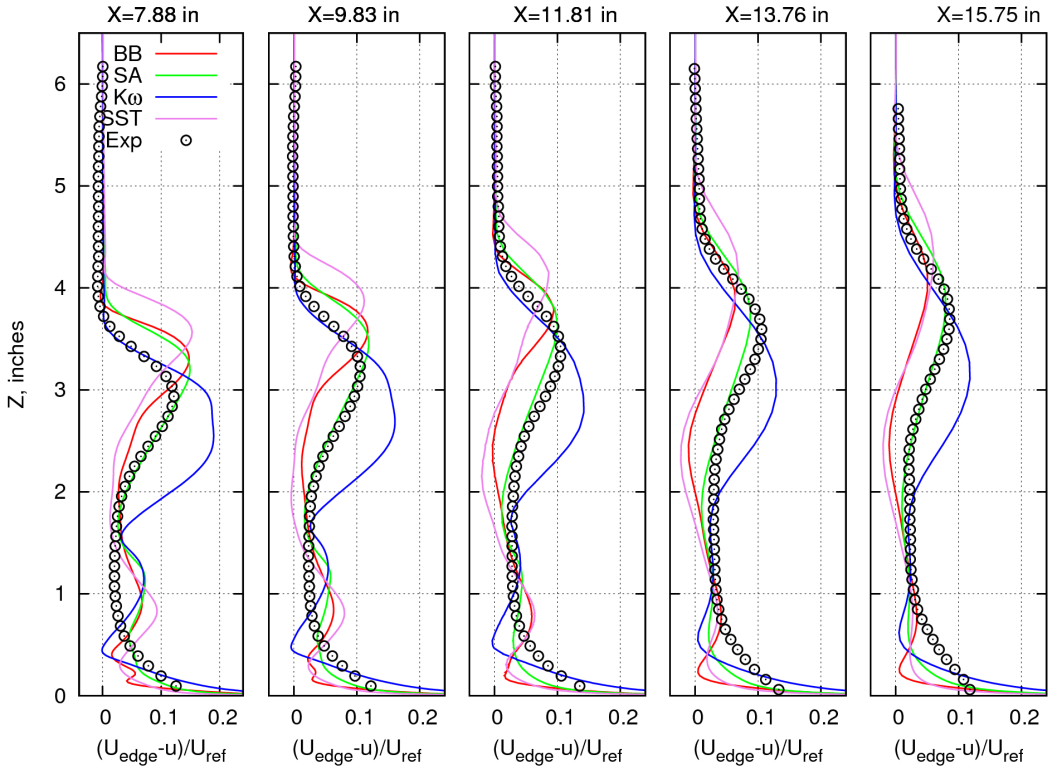

Figure 14. Velocity-deficit profiles for the different turbulence-model cases.

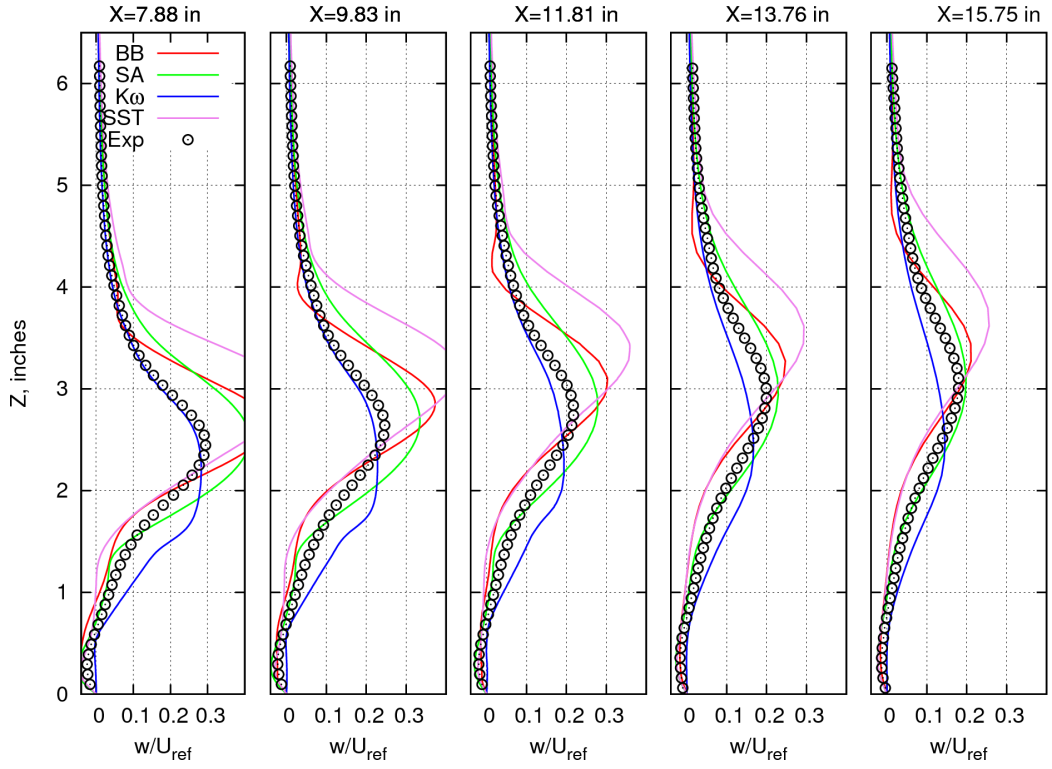

Figure 15. W-component of velocity profiles for the different turbulence-model cases.

suppresses the temporal terms, which could play an important role in the flow behavior. For this reason time-accurate cases were investigated. Second-order time-integration was used with dual time-stepping and ten inner-iterations per time step. A non-dimensional time step of 0.01 was used, this corresponds to a dimensional time-step size of $0.94x10^{-6}$ seconds. The ten inner iterations were enough to reduce the L_2 norm of the residual by three to four orders of magnitude in each zone during each time step. The initial conditions for each case was a converged, empty tunnel solution. A transient start-up procedure was used by linearly increasing the jet boundary conditions from zero flow to full strength over 400 time steps, or a time duration of $0.37x10^{-3}$ seconds. The SA cases were run over 36,000 time steps, for a total time duration of 0.034 seconds. The SST cases were run over 30,000 time steps, for a total time duration of 0.028 seconds.

The cases were run using the Spalart-Allmaras and the SST turbulence models. Both models were run with and without the detached-eddy simulation (DES) formulation.[23–25] A major short-coming of the RANS turbulence-modeling approach is the excessive production of turbulent eddy-viscosity in wake regions away from a wall. The DES is a hybrid approach which retains the RANS modeling close to the wall, and switches to large-eddy simulation (LES) away from the wall. This tends to reduce the turbulent eddy-viscosity in the wake regions. No modifications were made to the original grids for the DES runs. The original Cartesian grids may not be of optimal resolution for these DES runs, but are considered adequate for an initial assessment of the sensitivity to this approach.

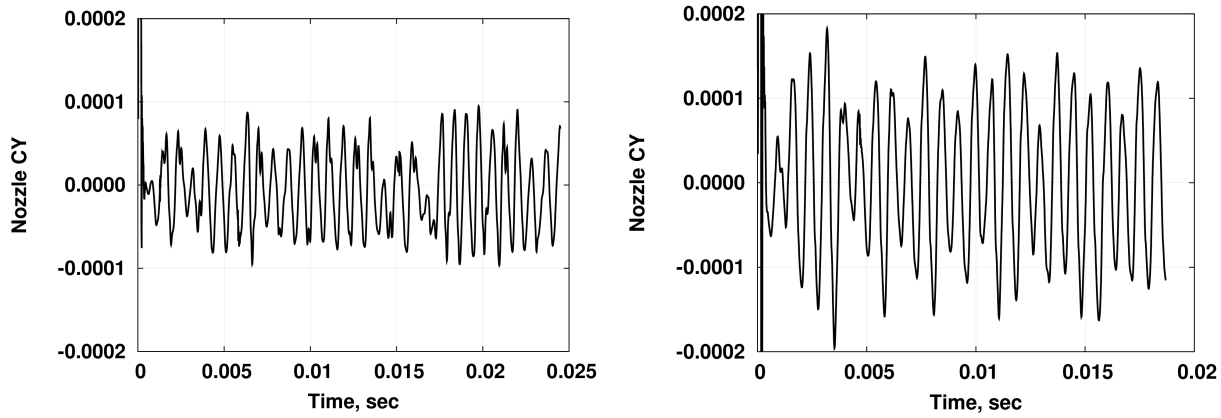

Figure 16. Time-history of nozzle CY for the SA and SST turbulence models.

The time-accurate SA and SST cases without the DES option both generated unsteady oscillating flows. Figure 16 plots the nozzle side-force coefficients versus time, which is a good indicator of the asymmetry in the jet plume. These plots indicate that both solutions appear to oscillate about a zero side force. A sequence of multiple timesteps of the iso-surface plus Mach contour plots for the SA case is shown in figure 17, and for the SST case in figure 18. These figures show that both cases develop a periodic oscillation of a similar frequency. The iso-Mach surfaces of the SST solution show a somewhat more complicated structure than the SA solution.

Figure 19 plots the nozzle side-force coefficient for the DES simulations using the SA and SST models. Mach contour plots for these cases are shown in figure 20 and figure 21. These figures show that the solutions tend to oscillate in time at a higher frequency with significantly more complicated flow structure in the plume and wake. The side-force oscillates about zero, and though does not appear to show a preference for either a positive or negative side force, the side-force history is not symmetric about zero. The contour plots show the presence of what Beresh at al. terms "wake vortices", which are vertical vortical structures which extend from the plume down to the wind-tunnel wall.

By averaging the unsteady solution data over time, it is found that the resulting solution is symmetric. Figure 22 shows the Mach iso-surface and contour plots for time-averaged solution data for all four of the time-accurate runs. These were averaged over the last 10,000 time steps of each run. It can be seen that the time-averaged solutions appear to be symmetric about the Y=0 plane.

Line plots of the velocity-deficit profiles and the z-component of velocity profiles are shown in figures 23 and 24, respectively. These profiles show some better agreement with the experimental results in the region closer to the wall for the DES cases. However, the DES cases overpredict the wake deficit. The DES cases

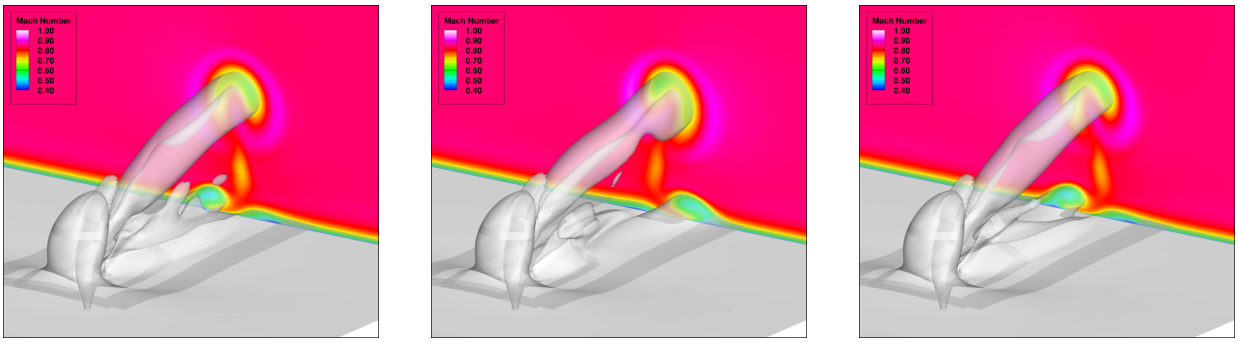

(a) 0.0186 seconds (b) 0.0190 seconds (c) 0.0193 seconds

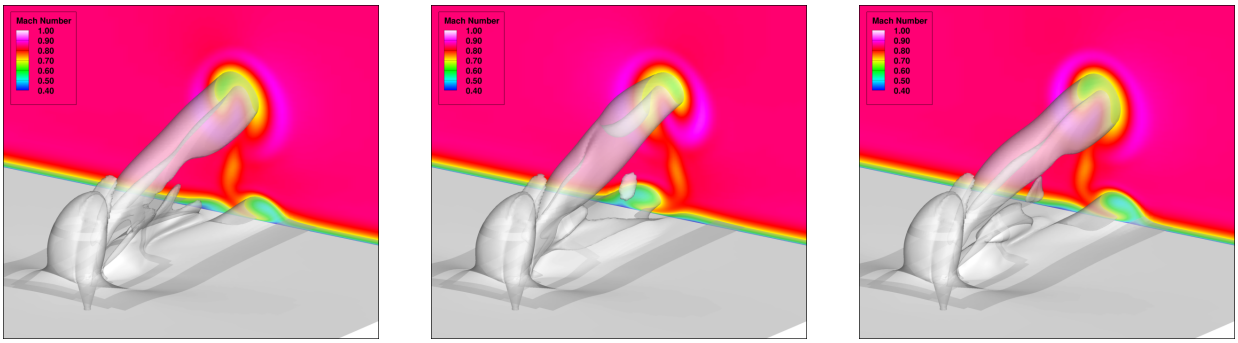

(d) 0.0196 seconds (e) 0.0200 seconds (f) 0.0204 seconds

Figure 17. Mach number contours at X=5.0 inches together with Mach=0.7 iso-surfaces for the time-accurate SA run.

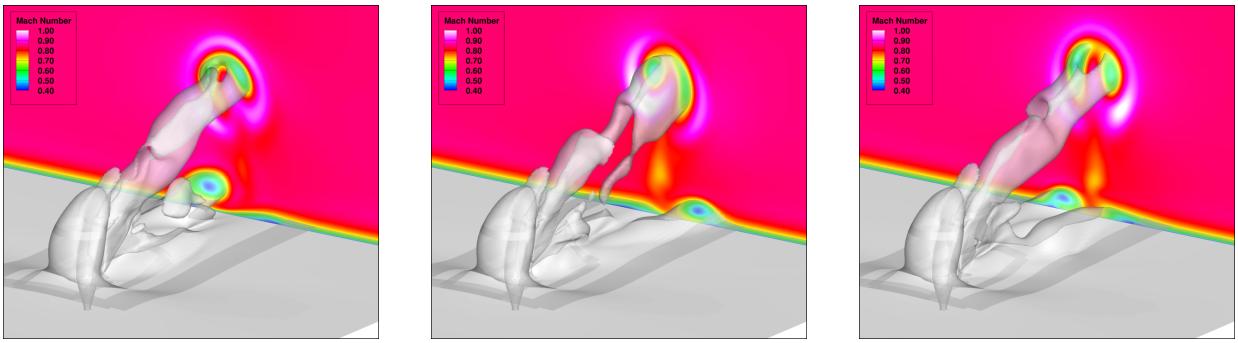

(a) 0.0146 seconds (b) 0.0151 seconds (c) 0.0155 seconds

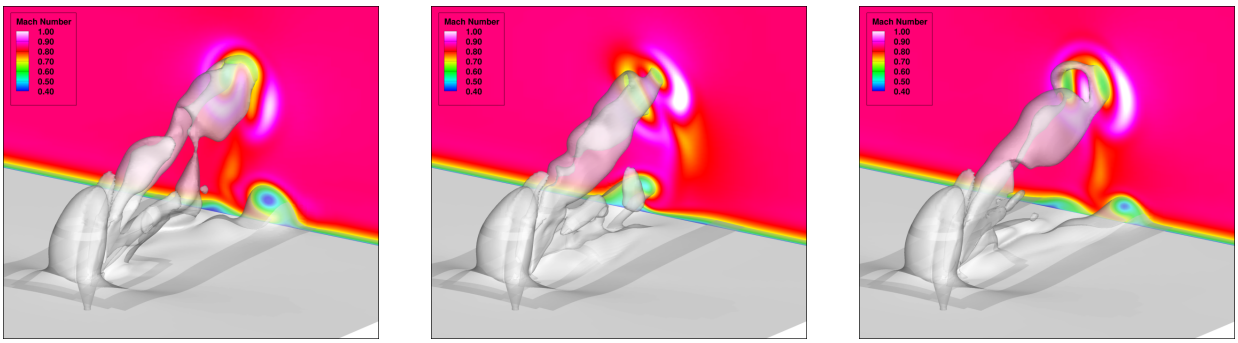

(d) 0.0158 seconds (e) 0.0161 seconds (f) 0.0165 seconds

Figure 18. Mach number contours at X=5.0 inches together with Mach=0.7 iso-surfaces for the time-accurate SST run.

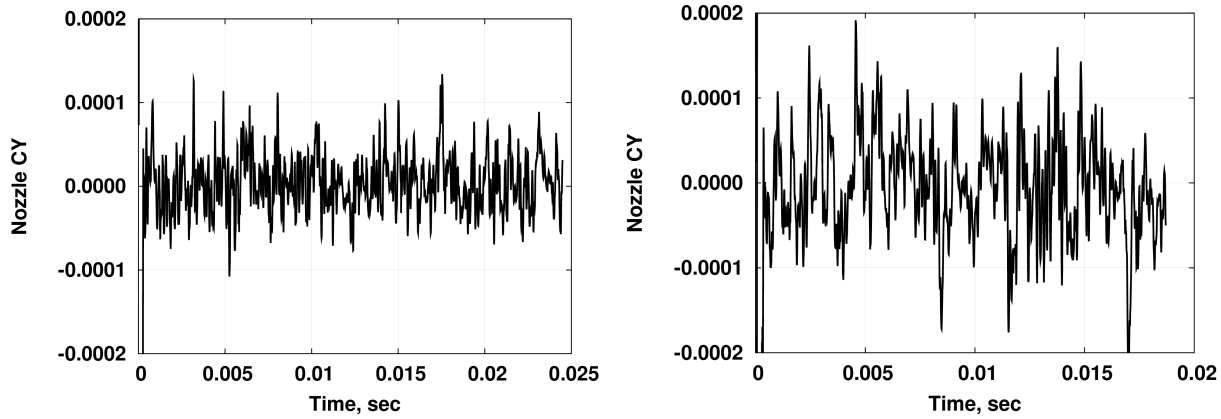

Figure 19. Time-history of nozzle CY for the SA and SST turbulence models with the DES terms.

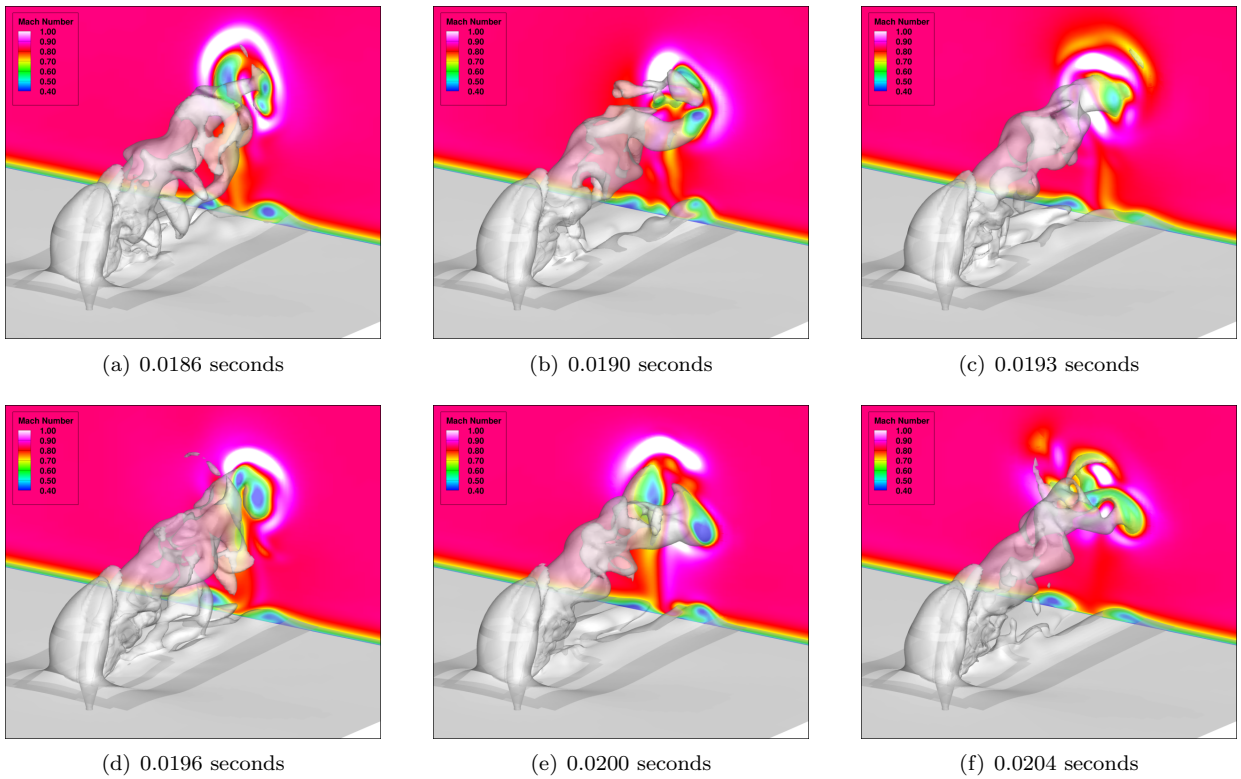

(a) 0.0186 seconds (b) 0.0190 seconds (c) 0.0193 seconds

(d) 0.0196 seconds (e) 0.0200 seconds (f) 0.0204 seconds

Figure 20. Mach number contours at X=5.0 inches together with Mach=0.7 iso-surfaces for the time-accurate SA with DES run.

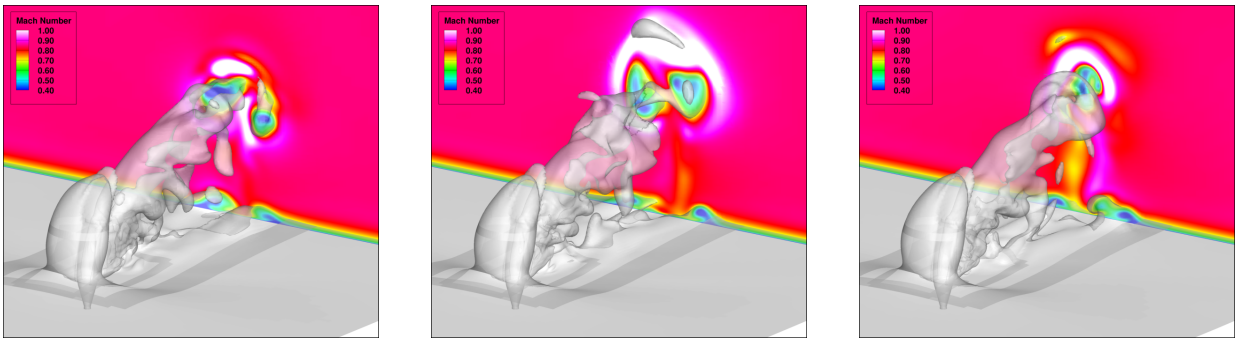

(a) 0.0146 seconds (b) 0.0151 seconds (c) 0.0155 seconds

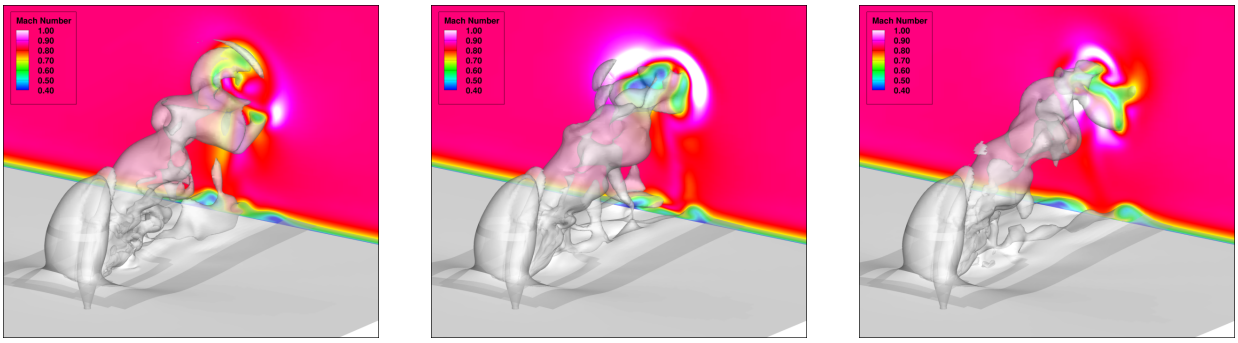

(d) 0.0158 seconds (e) 0.0161 seconds (f) 0.0165 seconds

Figure 21. Mach number contours at X=5.0 inches together with Mach=0.7 iso-surfaces for the time-accurate SST with DES run.

underpredict the maximum z-component of velocity, whereas the SST without DES overpredicts this velocity. Finally, it is noted that the time-averaged SA profiles look remarkably like the half-body SA results back in figure 7. These two sets of results are plotted together in figures 25 and 26. The solutions are very similar, with slight differences near the wall and in the wake.

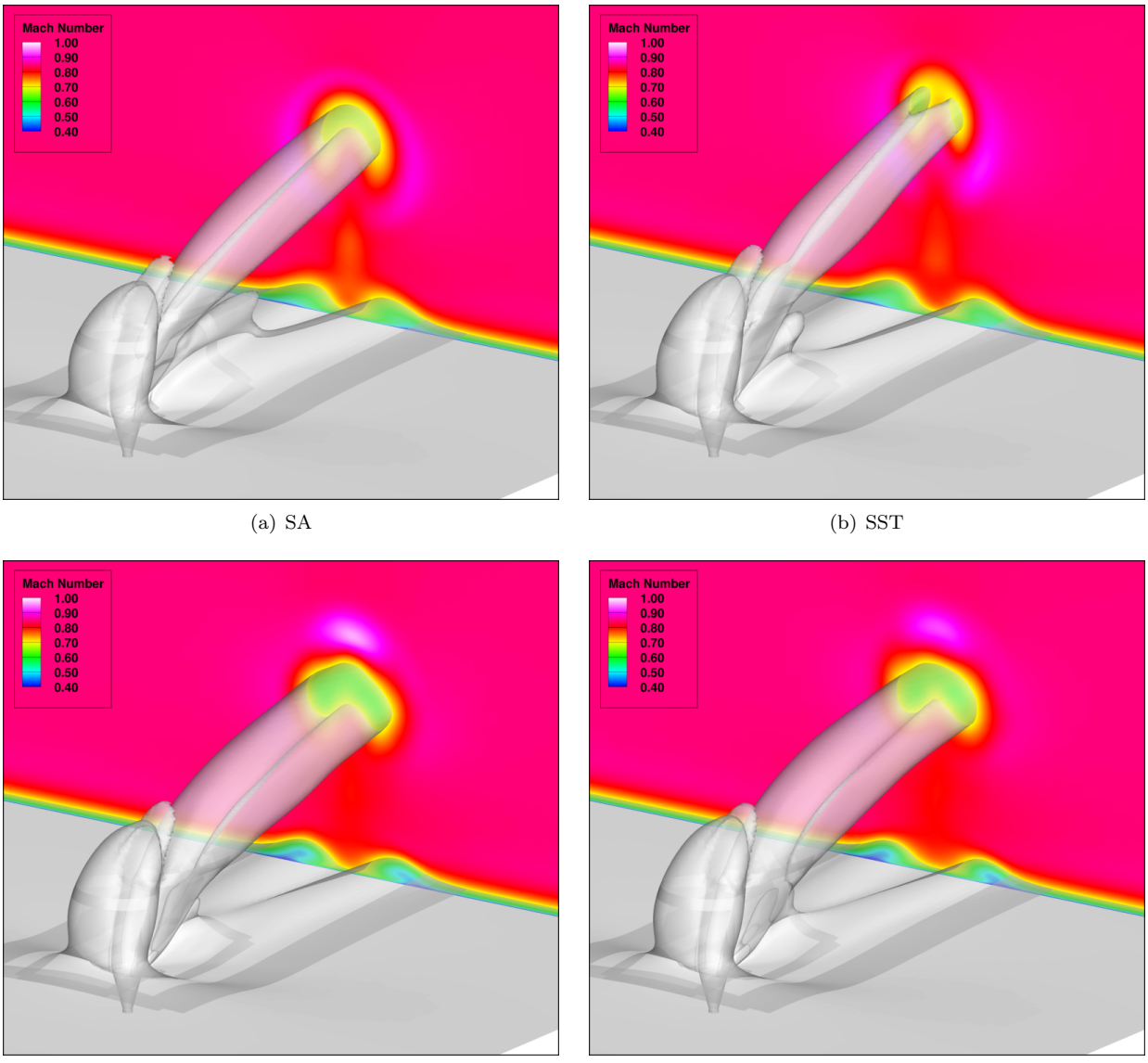

(a) SA

(b) SST

(c) SA + DES

(d) SST + DES

Figure 22. Mach number contours at X=5.0 inches together with Mach=0.7 iso-surfaces for the time-averaged solutions.

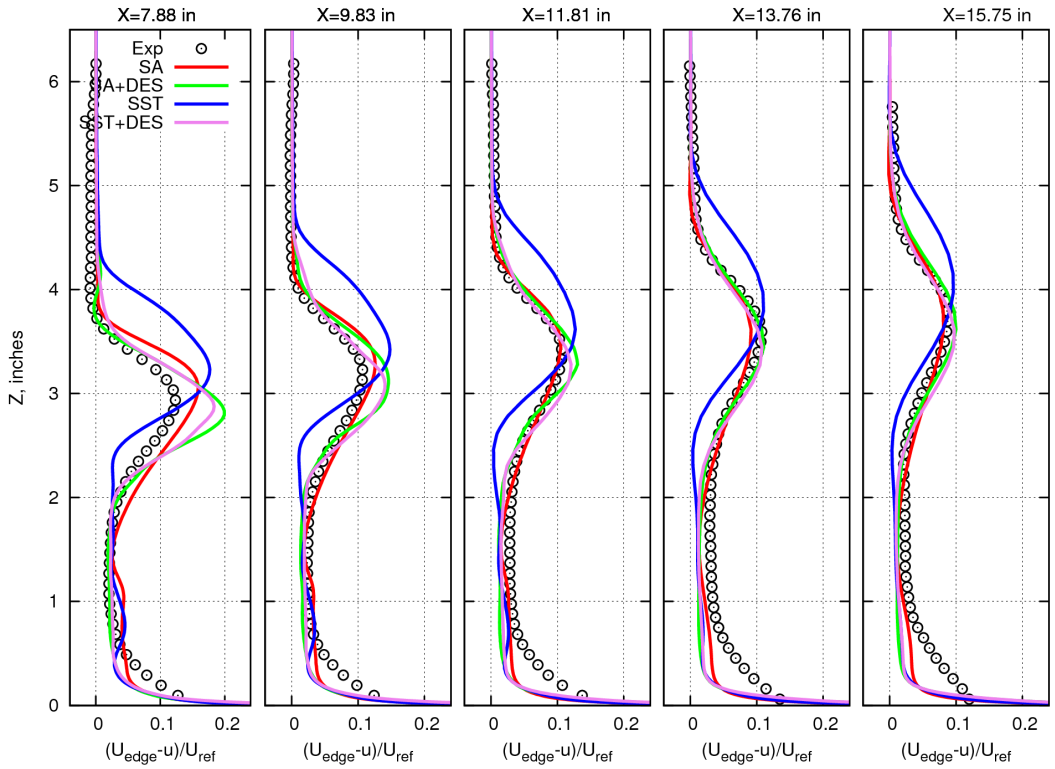

Figure 23. Velocity-deficit profiles for the time-averaged solutions.

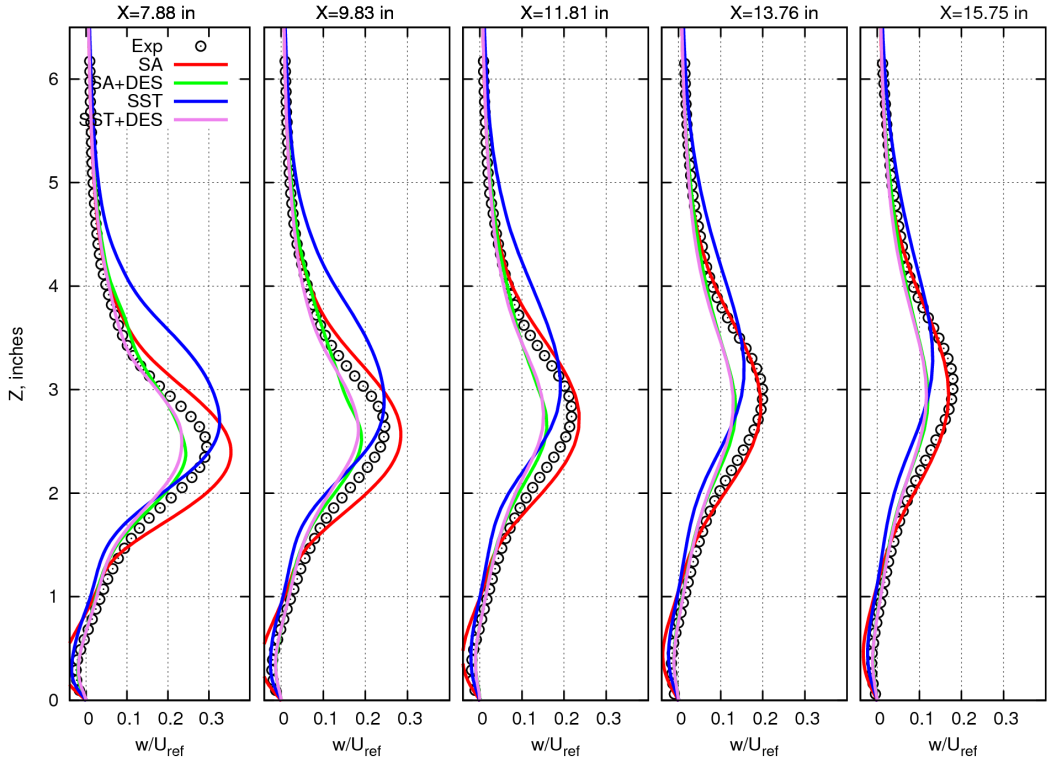

Figure 24. Z-component of velocity profiles for the time-averaged solutions.

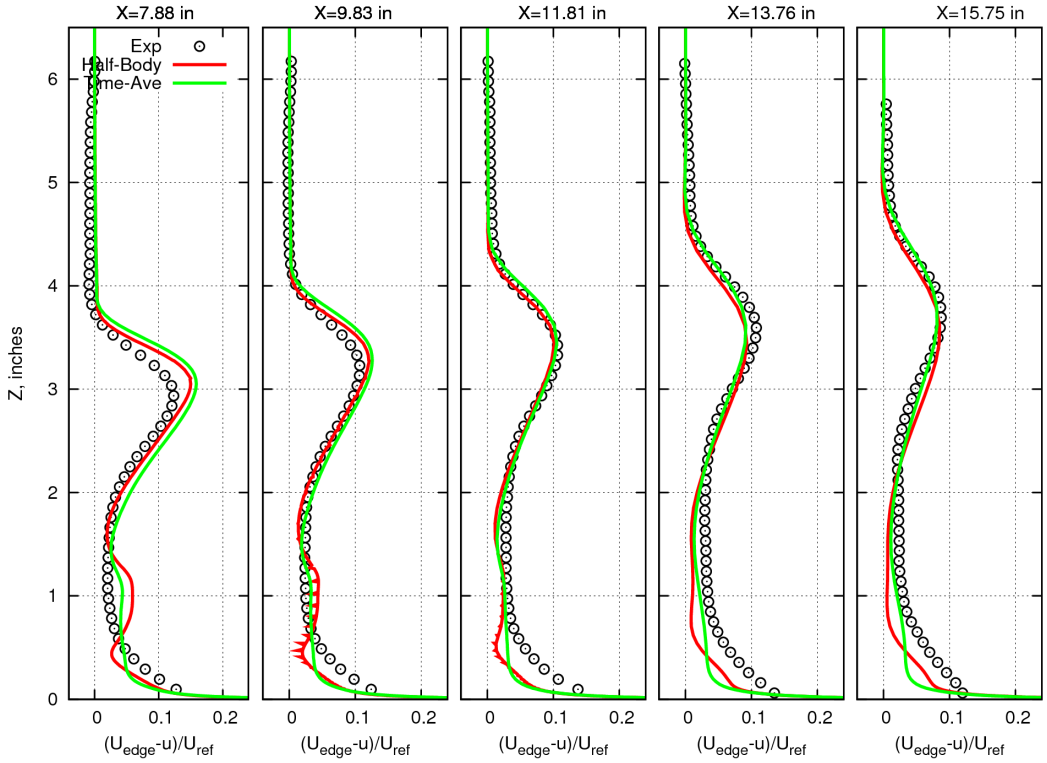

Figure 25. Velocity-deficit profiles for the SA model from the half-body case and the time-averaged solution.

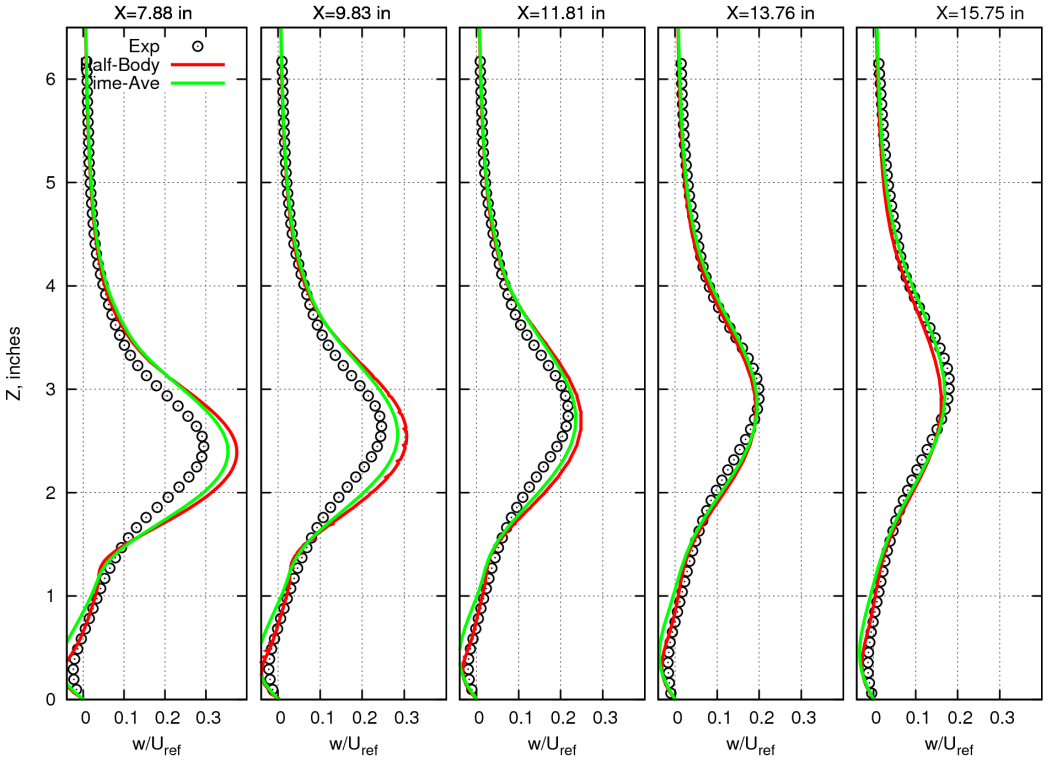

Figure 26. Z-component of velocity profiles for the SA model from the half-body case and the time-averaged solution.

III. LAV Simulations

The Orion LAV consists of a tower mounted tractor rocket attached to a shroud which covers the crew module. The function of the LAV is to carry the crew module away to safety in the unlikely event of a catastrophic failure during the vehicle's ascent. Figure 27 shows the location of the nozzles of the AM, ACM, and JM components on an earlier design of the Orion Pad-Abort test vehicle. During the powered portion of the abort, both the AM nozzles and the ACM nozzles are firing simultaneously, creating a significant amount of jet-plume interaction with the oncoming flow and the vehicle.

A. Overflow Inputs

For the LAV calculations, Overflow was run using the recommended input options from the project's simulation guidelines, which is presented together with validation data in the paper by Childs et al.[26] The inputs include using the HLLC upwind-differencing in Overflow together with the SSOR implicit scheme. The code was run in a steady-state mode using the SSOR implicit scheme, together with local time-stepping with a constant CFL number. All viscous terms, including cross terms, were enabled in the code. An extended slow start for the nozzle inflow boundary conditions, and enforcing a monotone update of the flow variables and CFL limits in expansion regions was used for these calculations. The flow fields were computed using the standard release version 2.1ae of the Overflow code. The computations were performed on the SGI Altix systems at the NASA Advance Supercomputing (NAS) known as *COLUMBIA*. This machine is an SGI Altix 3700 consisting of thousands of Intel Itanium-II CPUs. All of the runs used 128 CPUs, the SST turbulence model (without compressibility corrections), and the flow was assumed to be turbulent everywhere.

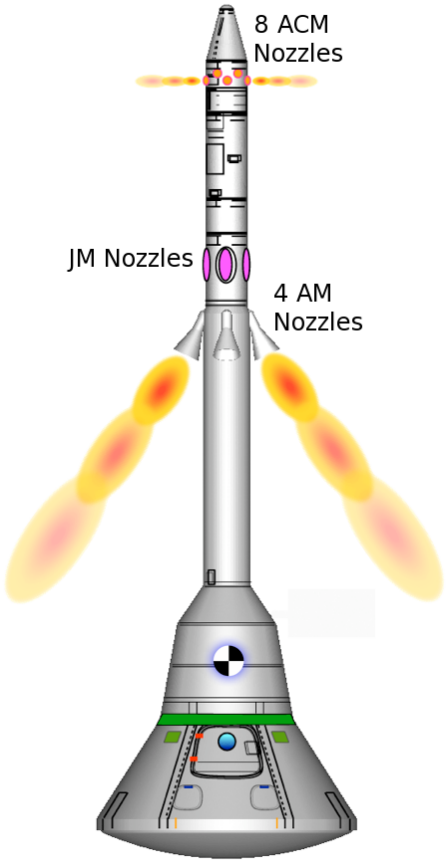

Figure 27. Drawing showing the major components of the Orion LAV.

Each case was run using a staged sequence of executions of Overflow. In the first stage, Overflow was run with FMG sequencing and three grid sequencing levels. The first FMG level used 2000 iterations and the second FMG level used 2000 iterations. The FMG sequence was followed by at least 2000 steady-state iterations. Some cases required another 2000 to 4000 iterations before they converged. The multi-grid option was turned off for all stages of the run sequence. A CFL number of 10.0 was used during all runs.

The multiple-species with variable γ option in the Overflow code was used. Three different gas species were used: the freestream air, AM exhaust gas, and ACM exhaust gas. This option in the code solves three extra species continuity equations to track the concentrations of each of the gases. The modeling uses only convection and ignores diffusion of the species concentrations. The ratio of the specific heat at constant pressure over the gas constant (C_P/R) is held constant and does not vary as a function of temperature.

B. Grid Generation

The overset grid system was generated using an automated grid-generation process based on the scripting system in the Chimera Grid Tools software package,[27,28] version 2.1. This script system automatically generates the surface and volume grids, generates input files for and executes pegasus5,[18] then generates the inputs files for Overflow and post-processing programs. The system also includes scripts to generate the powered-face boundary-condition files for the AM and ACM jets.

While there were many different ACM jet configurations simulated using the Overflow code, the primary configuration of interest in the current work uses two adjacent ACM jets turned on at full power, and with the AM firing at full power through all four AM nozzles. The grid system for this configuration included only the two power-on ACM nozzles, with the other ACM nozzles faired over to reduce the number of grid points required. Two grid zones were generated for each ACM nozzle: a cylindrical nozzle-fitted grid which wraps from the inside of the nozzle and up onto the outer surface of the LAV, and an overlapping grid inside the core of the nozzle, similar to the approach used in the jet-in-cross grid system. A companion power-off configuration grid system was also generated. The grid systems contained a total of 37 to 58 zones and 41.7 to 88.8 million grid points. There are approximately 33 million grid points in the abort motor plume refinement grids alone. Additional details of the grid-generation process is given in the paper by Childs et al.[26]

C. Computed Results

Computing the effect of the jet-interactions for a large number of configurations proved to be very challenging. While trying to cover a very large range of the parameter space, a number of non-linear behaviors have been uncovered. But perhaps the most interesting and challenging of the behaviors seen in the current work is that of an unexpected asymmetry in the wake of the ACM plumes at certain conditions. This asymmetry first showed up for some transonic conditions as a non-negligible side force and yawing moment in configurations that were symmetric about the pitch plane. This condition was most often observed when a pair of adjacent ACMs were firing on either side of the vehicle pitch plane. The source of the asymmetry was traced to a type of "bursting" or off-body flow reversal of the wake behind one of the ACM plumes. This bursting was characterized by a significant growth of the low-speed and reversed flow in the wake behind one plume, while the wake behind the other plume remained relatively energized with no reverse flow.

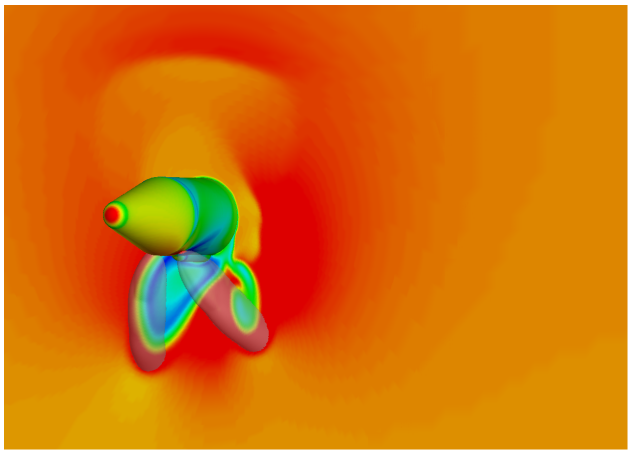

Figure 28. Mach contours in a cutting plane downstream of the ACM nozzles together with iso-surfaces of γ for Mach=1.10, α=0.

Figure 28 illustrates this flow asymmetry. This figure shows Mach contours in a cutting plane downstream of the ACM nozzles together with iso-surfaces of γ for a case run at Mach=1.10 and an angle of attack (α) of zero. This clearly shows that the wake behind the starboard ACM plume becomes much larger than on the port side. This asymmetry in the flow then interacts with the AM plumes which has an amplifying effect as the AM plumes interact with the capsule. The result is a significant side force and yawing moment, together with a significant nose-down pitching moment. This nose-down pitching moment acts counter to the intended pitching moment being generated by the firing of the two ACM jets in this configuration, and reduces the control authority of the vehicle at these conditions.

While asymmetric flows of this nature are not completely unexpected, every effort was made to ensure that this flow behavior was not due to faulty inputs, boundary conditions, thrust settings, or asymmetries in the geometry. All verification efforts showed that the asymmetry was not caused by such an input error. The development of the asymmetry during the transient start-up of the Overflow run was seen to develop early on during the FMG sequencing. Therefore, a number of different cases which exhibited the asymmetry were re-run without the FMG start-up sequence. Of these cases, a number of them converged to a symmetric solution. Others converged to the same asymmetric solution, and a few converged to mirror-image asymmetric solutions.

Figure 29 plots one of the original asymmetric solutions which was started with an FMG sequence at Mach=1.10, $\alpha = 0$. The figures shows contours of total pressure (C_{p0}) in a cutting plane beneath the ACM nozzles together with particle traces showing the flow in and around the ACM plumes. The traces show that the starboard-side ACM plume-wake has burst into a large region with reverse flow. The case run without FMG at the same conditions is shown in figure 30. This figure shows that the plume wakes are of nearly

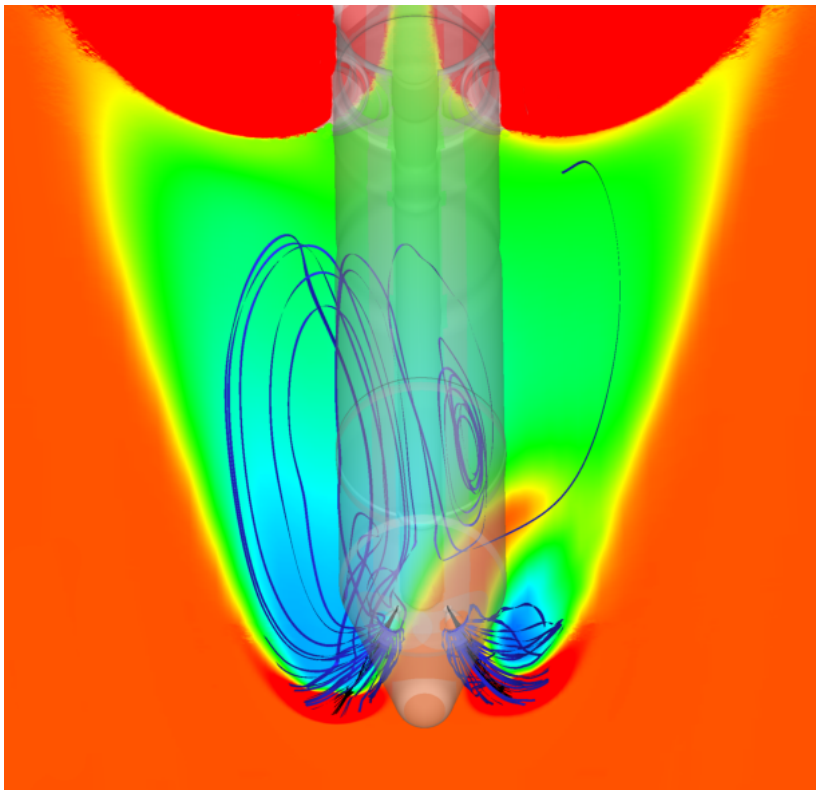

Figure 29. Cp0 contours in a cutting plane beneath the ACM nozzles and particle traces for FMG on, Mach=1.10, α=0.

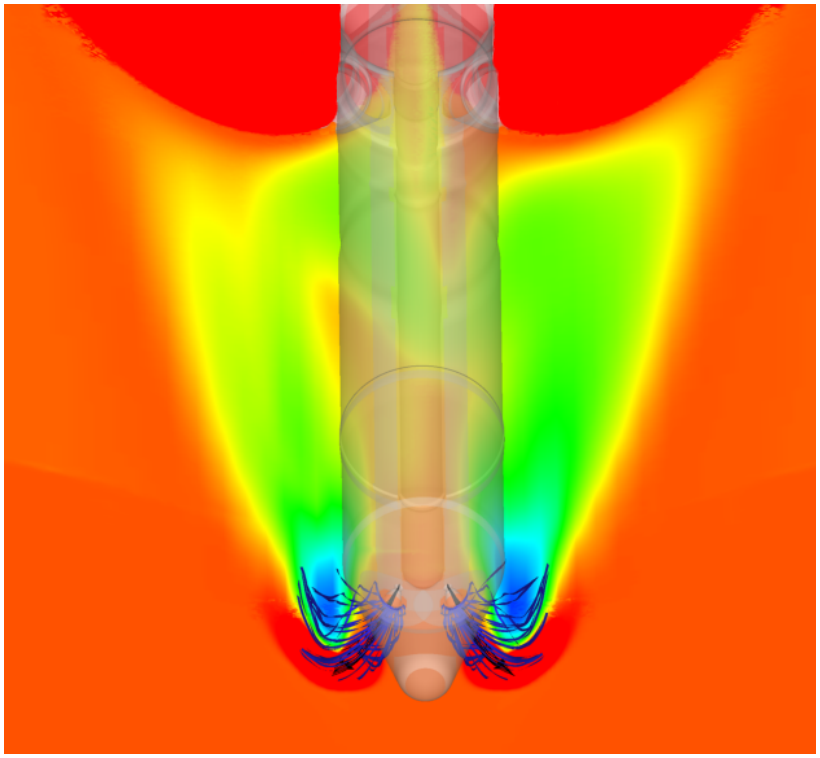

Figure 30. Cp0 contours in a cutting plane beneath the ACM nozzles and particle traces for FMG off, Mach=1.10, α=0.

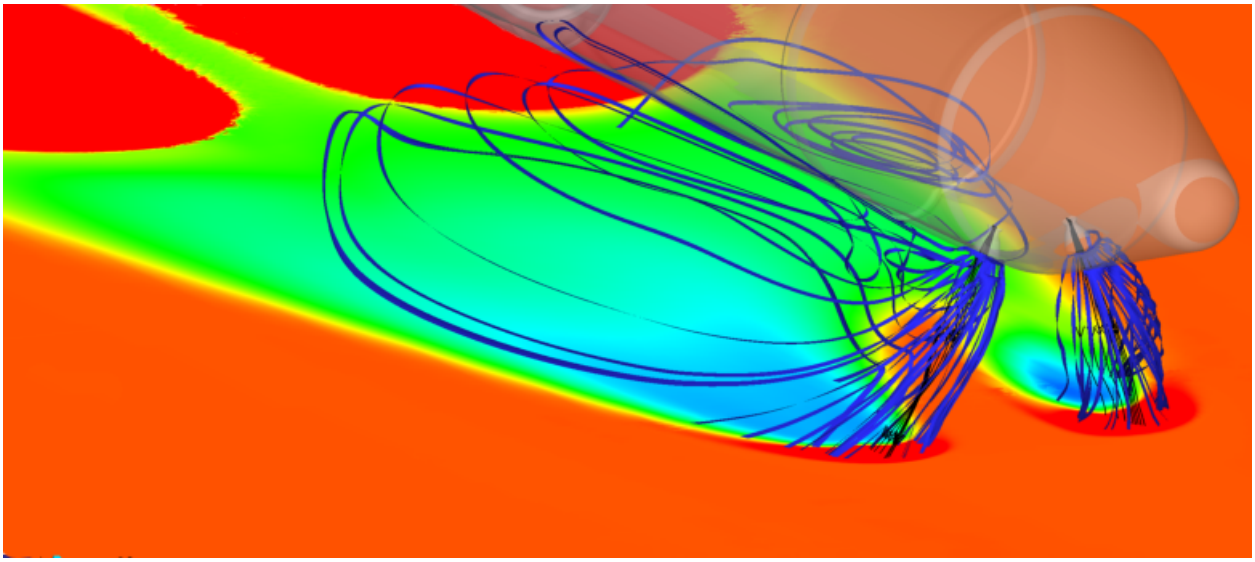

Figure 31. Cp0 contours in a cutting plane beneath the ACM nozzles and particle traces for FMG on, Mach=1.10, α=0.

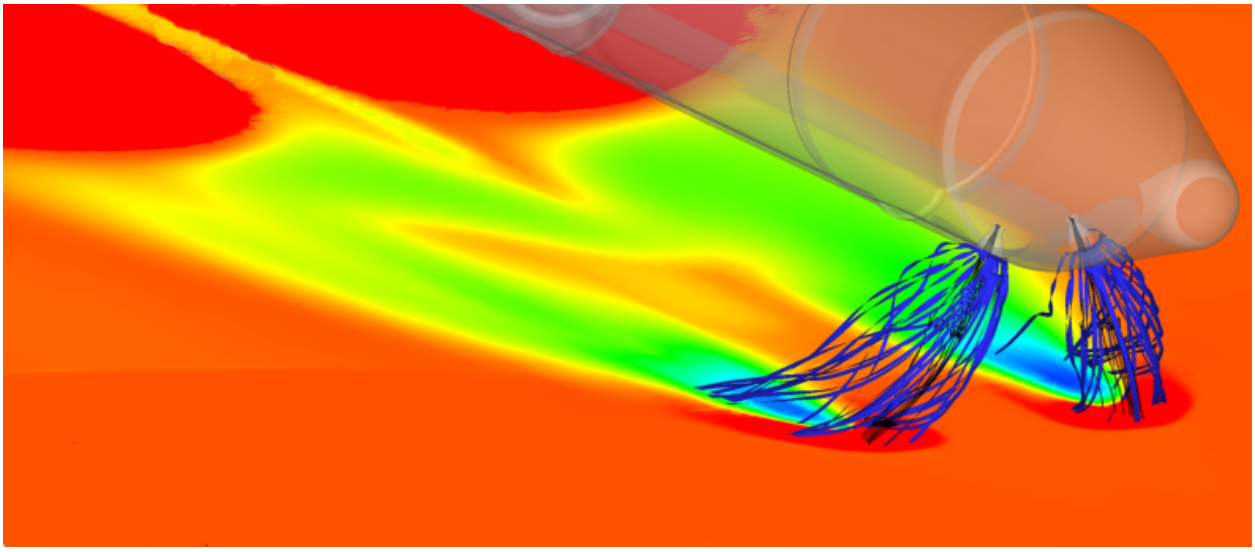

Figure 32. Cp0 contours in a cutting plane beneath the ACM nozzles and particle traces for FMG off, Mach=1.10, α=0.

the same strength without the same evidence of reverse flow. The same two plots are shown from different angles in Figures 31 and 32.

One of the cases in which the run without FMG produced a mirror image of the original asymmetric solution occurred at Mach=1.10, $\alpha = 10$ degrees. Figures 33 and 34 show both of these solutions. The first figure plots both the running side-force coefficient and the sectional side-force coefficient versus the axial location along the body. These two plots show that these two solutions are indeed nearly exact mirror images of each other. It also shows that the net side force comes from the jet interactions with the aft part of the vehicle. Figure 34 shows the running and sectional vertical-force coefficient versus axial location. This plot shows that these two solutions have the same vertical-force distribution, and that the vertical force pushes up on the aft part of the capsule which contributes to a a large nose-down pitching moment.

Finally, it is noted that the Cart3D code has also been used to compute the flow about the LAV for many of the same conditions as the Overflow simulations.[29] This code was recently used to run the same Mach=1.10 conditions with the same AM and ACM jet conditions cases that there were illustrated above. The Cart3D code also predicted the same type of asymmetric wake pattern behind the ACM plumes.[a] This provides further evidence that this asymmetric flow is a stable solution to the discretized Euler and/or Navier-Stokes equations.

IV. Acknowledgements

The authors wish to thank Steven Beresh of Sandia National Laboratories for providing his groups experimental data for the jet-in-crossflow. Thanks to Robert Childs of STC at NASA Ames, and to Noah Kim of Stanford University for reviewing this work and offering many helpful comments. The work documented herein was performed in support of the NASA Orion Multi-Purpose Crew Vehicle (MPCV).

V. Conclusion

Two different types of jet-flows have been computed using the Overflow code. The relatively simple flow of a supersonic jet in a subsonic cross-flow was used to validate the ability of the code to predict the downstream shape of the plume and its wake. These simulations produced asymmetric solutions for what is otherwise a symmetric problem. Extensive investigation into this behavior indicates that this jet does tend to have stable asymmetric solutions. Studies of the grid resolution, the choice of differencing scheme, and the choice of the turbulence model can affect the extent of the asymmetry, but it does persist for all these different approaches. Time-accurate computations were run, and these remained unsteady, exhibiting periodic behavior. The DES time-accurate runs captured more detailed small-scale structures in the flowfield. The time-averaged data from these solutions appeared to be symmetric. Future work with this flow problem is called for, with further comparisons to experimental data to be made, and further investigations into grid resolution and turbulence modeling.

The Overflow code has also been used to compute the flow around the Orion LAV with both AM and ACM plumes for a number of different conditions. Some of these solutions also produced an unexpected asymmetry in the flowfield that was attributed to an off-body flow reversal in one of a pair of ACM wakes. These asymmetric flow fields appear to be stable steady-state solutions to the numerical model of the LAV. These asymmetries may or may not be realizable in an actual flow field, and could be an artifact of the numerical scheme forcing a steady-state in which all temporal terms have been eliminated or damped out. This complex problem is a very challenging flow for which production steady-state RANS CFD is not yet up to the task of simulating accurately. The time-accurate jet-in-crossflow results provide motivation to run time-accurate simulations for some of the LAV ACM cases.

The current and future challenge will be to investigate the simpler problems such as the jet in crossflow and understand the physics well enough to devise a proper engineering approach that can be used to capture enough of the the relevant physics in order to reliably predict aerodynamic performance. In the case of the Orion launch-abort vehicle, some of the jet-interaction aerodynamics might require a time-accurate simulation of the accelerating vehicle because the flight conditions are changing very rapidly.

[a]Private communication with M. J. Aftosmis, NASA Ames Research Center, April 2010.

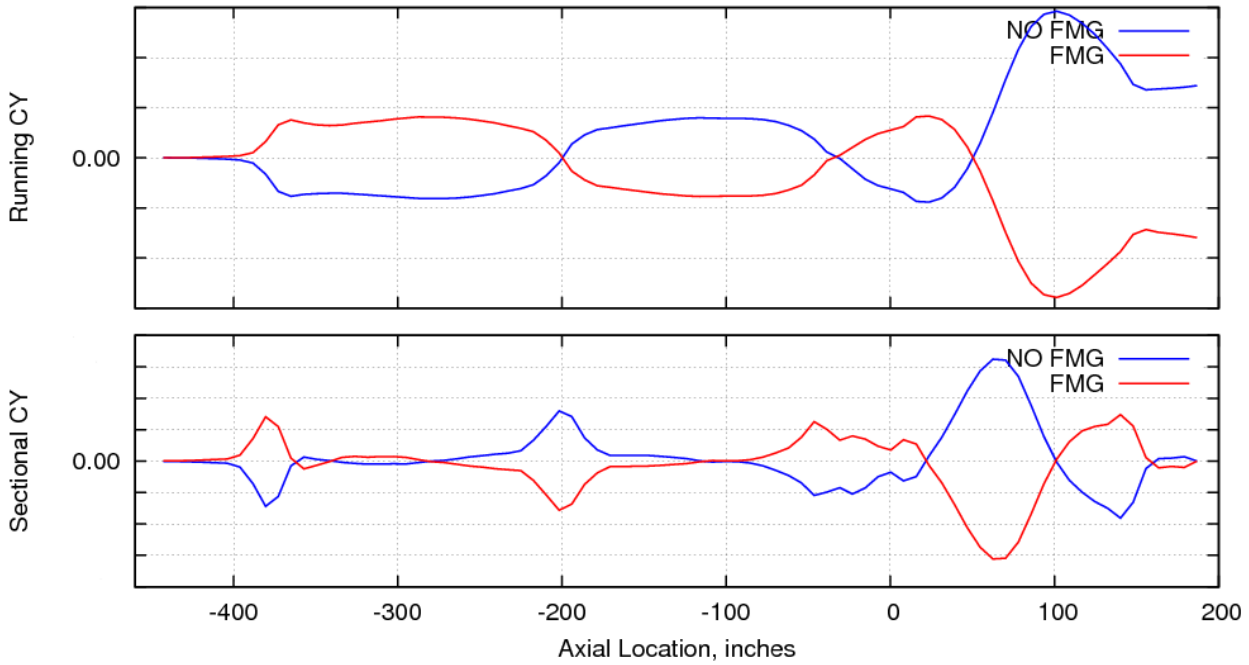

Figure 33. Mirror-image running and sectional side-force coefficients from the FMG-on and FMG-off solutions for Mach=1.10, α=10.

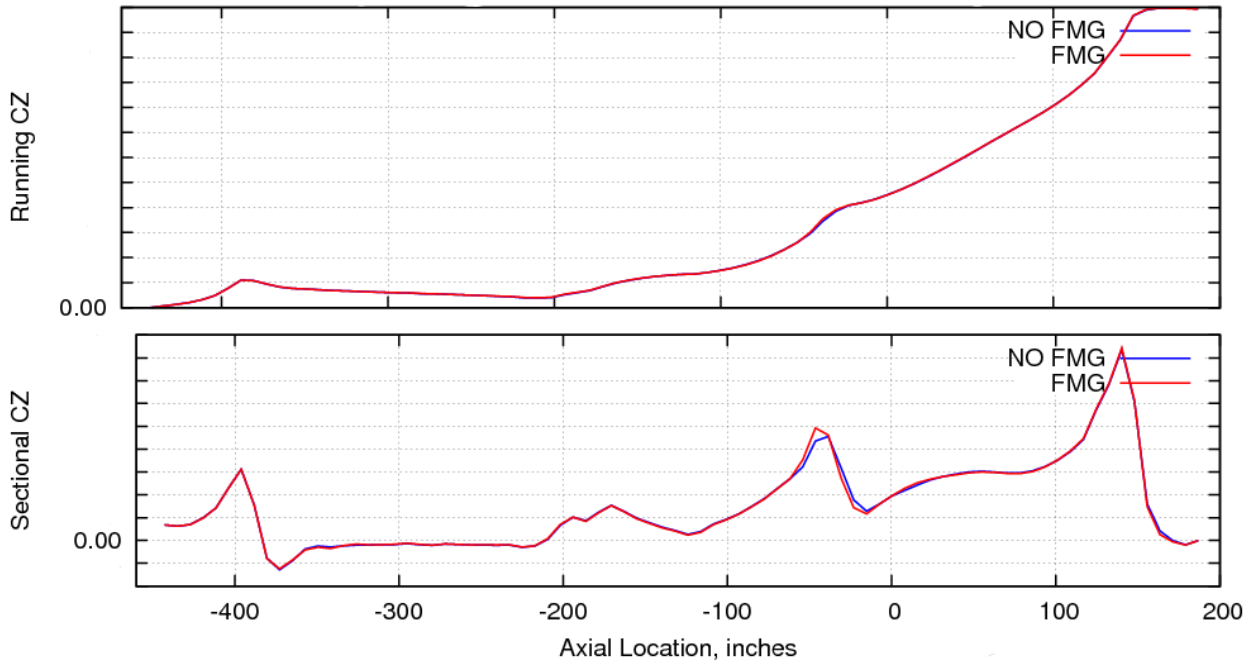

Figure 34. Running and sectional vertical-force coefficients from the FMG-on and FMG-off solutions for Mach=1.10, α=10, θ=0.

References

[1]Aftosmis, M. J., Berger, M. J., and Adomavicius, G. D., "A Parallel Multilevel Method for Adaptively Refined Cartesian Grids with Embedded Boundaries," Aiaa paper 2000-0808, Jan. 2000.

[2]Aftosmis, M. J., Berger, M. J., and Murman, S. M., "Applications of space-filling-curves to Cartesian methods in CFD," Aiaa paper 2004-1232, Jan. 2004.

[3]Berger, M. J., Aftosmis, M. J., Marshall, D. D., and Murman, S. M., "Performance of a New CFD Flow Solver Using a Hybrid Programming Paradigm," *Journal of Parallel and Distributed Computing*, Vol. 65, 2005, pp. 414–423.

[4]Aftosmis, M. J., Berger, M. J., and Melton, J. E., "Robust and Efficient Cartesian Mesh Generation For Component-Based Geometry," *AIAA Journal*, Vol. 36, No. 6, 1998, pp. 952–960.

[5]Mavriplis, D. J., Aftosmis, M. J., and Berger, M. J., "High Resolution Aerospace Applications Using the NASA Columbia Supercomputer," *International Journal of High Performance Computing Applications*, Vol. 21, No. 1, 2007, pp. 106–126.

[6]Buning, P. G., Gomez, R. J., and Scallion, W. I., "CFD Approaches for Simulation of Wing-Body Stage Separation," Aiaa paper 2004–4838, Aug. 2004.

[7]Jespersen, D. C., Pulliam, T. H., and Buning, P. G., "Recent enhancemnts to OVERFLOW," Aiaa paper 97–0644, Jan. 1997.

[8]Nichols, R., Tramel, R., and Buning, P. G., "Solver and Turbulence Model Upgrades to OVERFLOW 2 for Unsteady and High-Speed Applications," Aiaa paper 2006–2824, June 2006.

[9]Nichols, R., Tramel, R., and Buning, P. G., "Evaluation of Two Higher Order WENO Schemes," Aiaa paper 2007–3920, July 2007.

[10]Frink, N. T., Pirzdeh, S. Z., Parikh, P. C., Pandya, M. J., and Bhat, M. K., "The NASA Tetrahedral Unstructured Software System (TetrUSS)," *The Aeronautical Journal*, Vol. 104, No. 1040, 2000, pp. 491–499.

[11]Beresh, S. J., Henfling, J. F., and Erven, R. J., "Flow Separation Inside a Supersonic Nozzle Exhausting into a Subsonic Compressible Crossflow," *Journal of Propulsion and Power*, Vol. 19, No. 4, 2003, pp. 655–662.

[12]Beresh, S. J., Henfling, J. F., Erven, R. J., and Spillers, R. W., "Penetration of a Transverse Supersonic Jet into a Subsonic Compressible Crossflow," *AIAA Journal*, Vol. 43, No. 2, 2005, pp. 379–389.

[13]Beresh, S. J., Henfling, J. F., Erven, R. J., and Spillers, R. W., "Vortex Structure Produced by a Laterally-Inclined Supersonic Jet in Transonic Crossflow," Aiaa paper 2005–4653, June 2005.

[14]Beresh, S. J., Henfling, J. F., Erven, R. J., and Spillers, R. W., "Turbulent Characteristics of a Transverse Supersonic Jet in a Subsonic Compressible Crossflow," *AIAA Journal*, Vol. 43, No. 11, 2005, pp. 2385–2394.

[15]Beresh, S. J., Henfling, J. F., Erven, R. J., and Spillers, R. W., "Crossplane Velocimetry of a Transverse Supersonic Jet in a Transonic Crossflow," *AIAA Journal*, Vol. 44, No. 12, 2006, pp. 3051–3061.

[16]Beresh, S. J., Henfling, J. F., Spillers, R. W., and Erven, R. J., "Measurement of Experimental Boundary Conditions for CFD Validation of a Supersonic Jet in a Transonic Crossflow," Aiaa paper 2006–3449, June 2006.

[17]Spalart, P. and Allmaras, S., "A One Equation Turbulence Model for Aerodynamic Flows," *Recherche Aerospatiale*, Vol. 1, No. 1, 1994, pp. 5.

[18]Rogers, S. E., Suhs, N. E., and Dietz, W. E., "PEGASUS 5: An Automated Pre-processor for Overset-Grid CFD," *AIAA Journal*, Vol. 41, No. 6, 2003, pp. 1037–1045.

[19]Tramel, R. W., Nichols, R. H., and Buning, P. G., "Addition of Improved Shock-Capturing Schemes to OVERFLOW 2.1," Aiaa paper 2009-3988, June 2009.

[20]Baldwin, B. and Barth, T., "A One Equation Turbulence Model for High Reynolds Number Wall-Bounded Flows," Nasa tm 102847, Aug. 1990.

[21]Wilcox, D. C., "Multiscale Model for Turbulence Flows," *AIAA Journal*, Vol. 26, No. 11, 1988, pp. 1311–1320.

[22]Menter, F. R., "Zonal Two Equation k-ω Turbulence Models for Aerodynamic Flows," Aiaa paper 93-2906, July 1993.

[23]Spalart, P. R., Jou, W.-H., Strelets, M., and Allmaras, S. R., "Comments on The Feasibility of LES for Wings, and on a Hybrid RANS/LES Approach," *Advances in DNS/LES*, Greyden Press, Columbus OH, 1997, pp. 137–148.

[24]Spalart, P. R., "Strategies for Turbulence Modelling and Simulations," *International Journal of Head and Fluid Flow*, Vol. 21, 2000, pp. 252–263.

[25]Spalart, P. R., Deck, S., Shur, M. L., Squires, K. D., Streleta, M., and Travin, A., "A New Version of Detached-eddy Simulation, Resistant to Ambiguous Grid Densities," *Theoretical and Computational Fluid Dynamics*, Vol. 20, No. 3, 2006, pp. 181–195.

[26]Childs, R. E., Garcia, J. A., Melton, J. A., Rogers, S. E., Shestopovlov, A. J., and Vicker, D. J., "Overflow Simulation Guidelines for Orion Launch Abort Vehicle Aerodynamic Analyses," 29th aiaa applied aerodynamics conference, honolulu, hi, 27-30 june 2011, american institute of aeronautics and astronautics, reston, va (submitted for publication), June 2011.

[27]Rogers, S. E., Roth, K., Nash, S. M., Baker, M. D., Slotnick, J. P., Whitlock, M., and Cao, H. V., "Advances in Overset CFD Processes Applied to Subsonic High-Lift Aircraft," Aiaa paper 2000-4216, Aug. 2000.

[28]Chan, W. M., "The Overgrid Interface for Computational Simulations on Overset Grids," Aiaa paper 2002–3188, June 2002.

[29]Aftosmis, M. J. and Rogers, S. E., "Effects of Jet-Interaction on Pitch Control of a Launch Abort Vehicle," Aiaa paper 2008–1281, Jan. 2008.